In situ Investigation of Interphase and Microstructure effects on the Chemo-Mechanics of Thiophosphate Solid Electrolytes

Marm Dixit[1,+], Nikhilendra Singh[2,+], James P. Horwath[3], Pavel Shevchenko[4], Eric A. Stach[3,5], Timothy S. Arthur[*2], and Kelsey Hatzell[*1,6,7]

[1]*Department of Mechanical Engineering, Vanderbilt University*

[2]*Toyota Research Institute of North America*

[3]*Department of Material Science and Engineering, University of Pennsylvania*

[4]*X-Ray Science Division, Argonne National Laboratory*

[5]*Laboratory for Research on the Structure of Matter, University of Pennsylvania*

[6]*Interdisciplinary Department of Material Science, Vanderbilt University*

[7]*Department of Chemical and Biomolecular Engineering, Vanderbilt University*

[+]*equal contribution*

[*]*corresponding author: kelsey.b.hatzell@vanderbilt.edu, tim.arthur@toyota.com*

Abstract

Lithium thiophosphates (Li_3PS_4, LPS) are promising solid electrolytes for safe, energy dense solid-state batteries. However, chemo-mechanical transformations within the bulk solid electrolyte and at solid|solid interfaces can lead to lithium filament formation

and fracture-induced failure. The interdependent role of kinetically stable interphases and electrolyte microstructures on the onset and propagation of fracture is not clearly understood. Here, we investigate the effect of interphase chemistry and microstructure on the chemo-mechanical performance of LPS electrolytes. Kinetically metastable interphases are engineered with iodine doping and microstructural control is achieved using milling and annealing processing techniques. *In situ* transmission electron microscopy reveals how iodine diffuses to the interphase and upon electrochemical cycling pores are formed in the interphase region. Pores/voids formed in the interphase are chemo-mechanically driven via directed ion transport. *In situ* synchrotron tomography reveals that interphase pore formation drives edge fracture events which are the origin of through-plane fracture failure. Active Li metal has a tendency to fill the fracture region. Cycling lithium in fracture sites leads to localized stress within the solid electrolyte which accumulates and ultimately leads to catastrophic failure. Fractures in thiophosphate electrolytes actively grow toward regions of higher porosity and are impacted by heterogenity in solid electrolyte microstructure (e.g. porosity factor).

1 Introduction

All-solid-state batteries can enable energy dense anodes for next generation energy storage systems[1;2;3]. Solid electrolytes, such as thio-LISICONs, lithium–phosphorous–sulfur (LPS) glasses, and argyrodites (Li_6PS_5X, X=Cl, Br, I), with high ionic conductivity ($>10^{-3}$ S cm^{-1}) and low electronic conductivity ($\sigma_e \approx$ nS cm^{-1})[4;5] are especially promising for lithium metal solid state batteries. However, despite excellent transport properties, the electrode|solid electrolyte chemo-mechanical stability remains a significant challenge[2;6].

Most inorganic solid electrolytes (ISE) are reactive with Li metal and form an interfacial decomposition product or interphase region. There are three prominent types of Li|SE interphases: (1) thermodynamically or kinetically stable (non-reactive), (2) unstable (reactive)[7;8], and (3) kinetically metastable (Fig. 1a)[9]. Few solid electrolytes are non-reactive with lithium metal, with Garnet-type LLZO ($Li_7La_3Zr_2O_{12}$) being a possible exception[10;11]. NASICON-type solid electrolytes (LAGP, LATGP, etc.) are examples of reactive electrolytes that form a mixed (ionic/electronic) conductivity interphase[7]. Finally, several types of solid electrolytes are metastable and form an interphase that is electronically insulating and ionically conducting. Li_3PS_4, for examples, is kinetically metastable as the interphase is primarily composed of electrically insulating lithium sulfide (Li_2S) and lithium phosphide (Li_3P)[9;12;13]. While interphase structure, composition, and properties are not well understood, interphase growth leads to greater cell polarization[14;15]. The microstructure and transport properties of the interphase can lead to non-uniform current densities, low power density, and local stress generation at buried electrode|electrolyte interfaces[16;17]. The latter can result in catastrophic failure via lithium filament formation, electrical shorting, and fracture[18].

Active or passive approaches during electrolyte synthesis and processing are commonly utilized to control interphase properties. Active approaches include the use of an interlayer barrier film[19;20;21;22]. Prior studies have investigated atomic layer deposition of interlayer materials (Al_2O_3, Si, $Li_xAl_{(2-x/3)}O$, $LiXO_3$(X = Ta, Nb)) to improve the surface wetting capability of metallic lithium and lower interfacial resistances[23;24;25]. Passive approaches such as halide doping or substitution have been reported to increase the stability of sulfide containing electrolytes with lithium metal through the formation of a nanometer-thin passivating interphase[26;27]. Halide doping has also been reported to improve the ionic conductivity, wet-

3

tability with the Li metal as well as the electrochemical stability window[5;28;29;30;19;31;32;33]. Theoretical and experimental studies ascribe this increase in performance to the formation of an ionically conducting interphase with Li_2S, Li_3P and LiI[19]. While transport in the interphase undoutedbly plays a role on performance, it is less clear how the chemo-mechanics of the interphase governs performance. Stress within individual battery components and/or at interfaces can occur because of physical volume change, the formation of gas, and/or mass (ion) transport. While concentration gradients do not exist in a single ion conducting electrolyte, there is the potential for stress-assisted diffusion at solid|solid interfaces[34]. Irregular interphase growth or Li^0 electrodeposition can lead to stress gradients in a solid electrolyte and alter the local energy level of the cation and contribute to directed ionic transport[35;36]. Mechanical stresses can also affect the dissolution and deposition kinetics governed by molar volume mismatch between solid electrolyte and lithium metal electrode[35]. These chemo-mechanical effects can lead to non-uniform ionic flux at electrode|solid electrolyte interface and be a driver for mechanical degradation.

The interdependent relationship between local ion transport, electrode|electrolyte contact, and solid electrolyte mechanical properties and cycle life is important for resilent solid state batteries. Thiophosphate solid electrolytes with halide substitution and/or doping have lower mechanical properties (Young's modulus) which enables soft interfaces, better contact with metallic lithium, and longer cycle lifetime[37]. A low Young's moduli (≈ 18 GPa[38]) can mitigate stress generation resulting from elastic mismatch at an interface. However, thiophosphate solid electrolytes have a low fracture toughness (≈ 0.2 MPa m$^{\frac{1}{2}}$) and are prone to fracture[38;39]. Prior work on the NASICON family of solid electrolytes has suggested that interphase instability can lead to non-uniform stress distribution which initiates fracture-

induced failure[40]. Other works suggest that operating conditions[41;42;43] or the bulk solid electrolyte[44;16;45;46;47;48] may be origins for fracture. However, the influence of electrolyte microstructure heterogeneity on stress distribution and fracture mechanics is not well known. This lack in understanding is primarily because there are limited experimental techniques capable of probing these dynamics at buried interfaces. One technique capable of *in situ* characterization of solid state batteries is synchrotron x-ray computed tomography (XCT) which offers resolutions $\sim 1\ \mu$m. This resolution range is ideal for the detection of mesoscale material transformations in solid-state batteries[49]. Recently, *ex situ* studies revealed that pore connectivity in garnet-type oxides correlated with obtainable critical current densities[47;50]. Furthermore, XCT has revealed that mechanical deformation and irregular contact at electrode|electrolyte interfaces may drive filament propagation in Na^+ β-alumina and LPS electrolytes respectively[51;52]. Failure mechanisms transcend several length-scales, from nano-scale interfacial reactions to meso-scale crack and fracture propagation. Furthermore, these occur at disparate time scales which complicates experimental assessment[53]. Combining electrochemical measurements with (non-destructive) characterization techniques is crucial for deconvoluting the nature of chemo-mechanics in solid state battery systems[54].

Herein, we systematically study material transformation pathways which impact fracture in a series of thiophosphate solid electrolytes in order to understand the nature of interphase chemistry and microstructural heterogeneity on fracture. Thiophosphate solid electrolytes are systematically altered for interfacial chemistry (via halogen doping) and microstructural heterogeneity (milling and annealing). A multi-modal approach is employed to elucidate the role solid electrolyte microstructure and interphase impact fracture events. *In situ* transmission electron microscopy provides evidence for interphase formation mechanisms and provides

nano-scale insight into pore formation in the interphase which drives edge fracture degradation modes at solid electrolyte|lithium interfaces. *In situ* synchrotron X-ray tomography experiments resolve fracture growth mechanisms. Fracture pathways in solid electrolyte are correlated with microstructure heterogeneities. The results demonstrate that the temporal onset of fracture is governed by interphase properties. However, the fracture-type was seen in all electrolytes independent of the interphase and the extent of fracture correlated well with microstructure heterogeneity. These local cracks are filled with electrochemically active Li metal. The active Li metal in the cracks can be cycled and thus contribute to localized stress within the solid electrolyte which accumulates and ultimately leads to catastrophic failure by fracture.

2   Results and Discussion

Mechanical failure in thiophosphate solid electrolyte manifests as cracks that traverse through the bulk of the material (Fig. 1b). Crack propagation through the bulk is spatially non-uniform in terms of density and morphology. The material properties of the solid electrolyte (microstructure, density, interphase structure, etc.) can influence fracture events. Herein, we investigate a series of thiophosphate solid electrolytes with varying microstructures and interphase properties to assess the impact on mechanical failure (Fig. 1c). A–LPS is an amorphous sulfide glass-ceramic electrolyte (Li_3PS_4) that is kinetically unstable and can form an lithiated interphase composed of Li_2S and Li_3P byproducts. An interphase can lead to an increase in cell polarization with cycling and cell failure. Extensive interfacial decomposition of A–LPS upon contact with metallic lithium is observed from tomography experiments

6
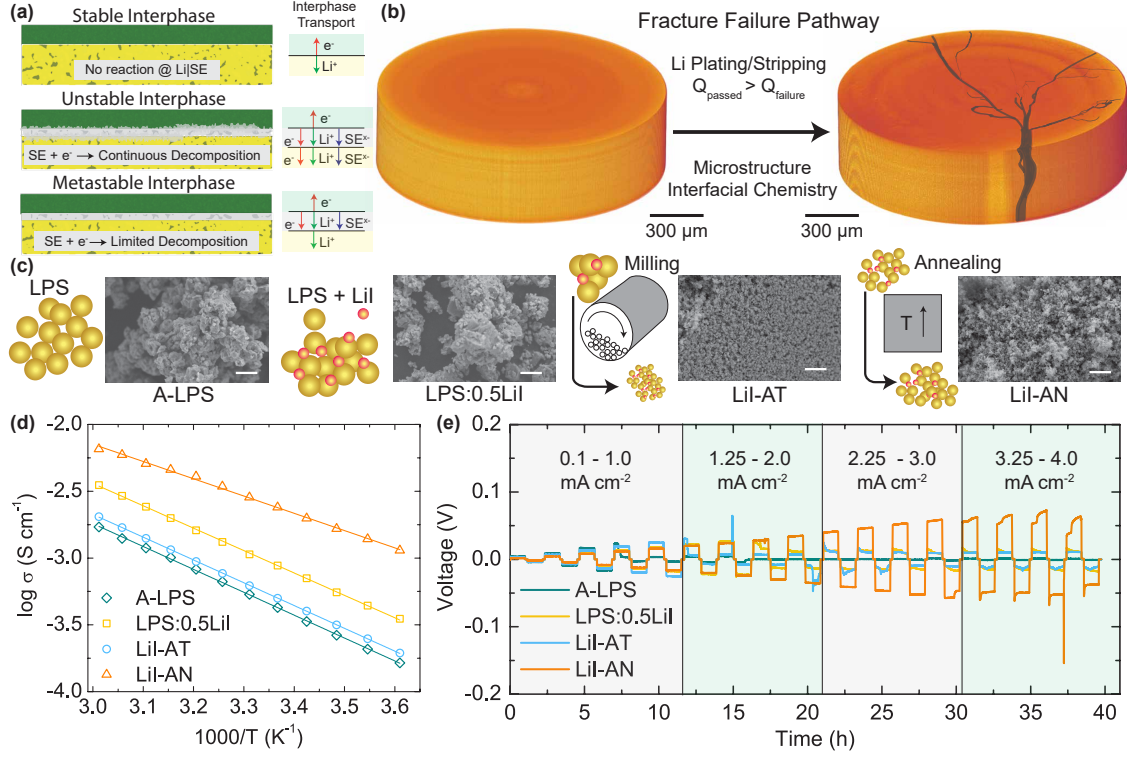
Figure 1: Investigation of Material Transformations in LPS Material. (a) Schematic diagram depicting Li metal and solid electrolyte interphase types. Stable interphase has no chemical decomposition of SE; unstable interphase shows continuous SE decomposition while kinetically metastable interphase shows controlled SE decomposition. Corresponding ionic and electronic conduction behavior are also indicated. (b) 3D tomography reconstruction of pristine and failed LPS electrolyte pellet. Effect of interfacial chemistry and microstructure on mechanical failure in LPS materials is investigated. (c) SEM images of powder materials in the study along with schematic diagrams highlighting processing used to synthesize the material. The scale bar on all images is 10 μm. A–LPS is amorphous sulfide material. LPS:0.5LiI is a mixture of amorphous LPS and LiI salt. LiI–AT material is obtained by mechanical milling of the LPS:0.5LiI material. LiI–AN is obtained by annealing the LiI–AT material. (d) Ionic conductivity, and (e) critical current density measurement for the solid electrolytes.

and is evidence of an unstable interphase (Fig. S1a-b). Solid electrolytes with kinetically metastable interphases can be obtained by doping LPS with LiI. LiI addition leads to higher mobile Li^+ concentration as well as interfacial decomposition to ionically conducting LiI along with the typical LPS decomposition products (Li_2S and Li_3P) . Thus, the ion conducting interphase coupled with better Li wettability contributes to better anode stability in the iodine-doped LPS (LPS:0.5LiI)[19;30;31]. In order to systematically change the microstructure of LPS:0.5LiI, two different post processing techniques were utilized. First, the LPS:0.5Li solid electrolyte was milled in order to reduce the primary particle size and improve the packing density (LiI–AT). Subsequently, the milled powders were annealed which resulted in a nano-crystalline phase with higher densification and lower porosity (LiI–AN). All samples studied (A–LPS, LPS:0.5LiI, LiI-AT, LiI-AN) show characteristic diffraction patterns resembling an amorphous structure (Fig. S2). LiI addition induces some crystallinity in the samples. A–LPS material shows a porous structure with pores sizes >3-5 μm (Fig. S3). LPS:0.5LiI, LiI–AT and LiI–AN show consistently decreasing porosity and pore sizes (Fig. S3). Energy dispersive spectroscopy mapping of pellets reveals a uniform iodine distribution on all doped samples (Fig. S4).

The room temperature ionic conductivity increases as A–LPS<LiI–AT<LPS:0.5LiI<LiI–AN (Fig. 1d, 4.26×10^{-4}, 5.01×10^{-4}, 8.79×10^{-4}, 2.40×10^{-3} S cm^{-1}, respectively). The corresponding activation energy for the materials are 0.111, 0.144, 0.147, and 0.148 eV for LiI–AN, LPS:0.5LiI, LiI–AT, and A–LPS. LiI–AN shows almost a 5× increase in ionic conductivity and a 25% reduction in the activation energies compared to the amorphous material. Long-range order as well as the particle-particle adhesion in the material is improved in a dense matrix leading to improved ion transport properties[44]. Reduction of ion-blocking

pores can also contribute to improved ion transport properties (low tortuosity)[50] and iodine doping increases the concentration of mobile Li$^+$ ions and reduces interactions with the glass network leading to improved ionic conductivity[31].

The critical current density (CCD) and cumulative charge passed before failure (charge-to-failure) follows a similar trend to the ionic conductivity (Fig. 1e) with LiI–AN showing a maximum CCD of 4 mA cm^{-2} (135.72 C cm^{-2}), and A–LPS showing the minimum CCD of 0.75 mA cm^{-2} (6.849 C cm^{-2}). LiI–AT fails at 1.25 mA cm^{-2} (19.62 C cm^{-2}) and LPS:0.5LiI fails at 1.75 mA cm^{-2} (41.67 C cm^{-2}). Halogen-doped solid electrolytes (LPS:0.5LiI,LiI–AT and LiI–AN) demonstrate an increased CCD compared to the undoped solid electrolyte (e.g. A–LPS). Considering current limit diagrams based on nucleation theory, the critical current density is given as[55],

$$j^* = \frac{(2\gamma\Omega_{Li}/r_c) + \sigma_F\Omega_{Li}}{fd(1-\alpha)|e|} \cdot \frac{1}{\rho} \tag{1}$$

where j^* is the critical current density, γ is the specific energy of the interface , Ω_{Li} is the volume per Li atom in the electrolyte, r_c is the critical radius, σ_F is the fracture stress, f is the contribution of grain boundary resistivity, d is the grain (particle/feature) size, α is the ratio of grain boundary to grain (void/particle) size, e is the charge on the electron, and ρ is the overall resistivity. The critical current density (j^*) is proportional to the ionic conductivity and inversely proportional to the total resistivity. Highly dense LiI–AN with higher ionic conductivity shows improved critical current density as well as charge-to-failure over the other halogen containing materials (LiI–AT, LPS:0.5LiI). Increased particle surface area in the LiI–AT material compared to the LPS:0.5LiI material can lead to a higher effective grain boundary resistance for the milled material. This results in a lower ionic

conductivity and critical current density for LiI–AT compared to LPS:0.5LiI. Interfacial effects of halogen doping can also aid in improving the critical current density. Uniform contact between the plating/stripping surface of the Li metal anode and the electrolyte leads to planar Li plating and stripping. Iodine can potentially act as a protective layer to ensure a congruent, contiguous interface between LPS and Li metal while also preventing the continuous decomposition of LPS in contact with Li metal.

A nanoscale understanding of interphase compositional and morphological transformations during electrochemical cycling is challenging because there are limited non-destructive techniques capable of probing these interfaces with adequate spatial and temporal resolutions. *In situ* TEM (Fig. 2, S5) is implemented to assess the chemo-mechanical response of the solid electrolyte during lithium stripping and plating. The solid electrolyte was benchmarked with *ex situ* experiments described in the supporting methods section, to ensure solid electrolyte stability for *in situ* studies. Li metal was placed on a metal probe while the solid electrolyte (LPS:0.5LiI) was mounted on a Cu TEM half-grid (Fig. 2a-c). LPS:0.5LiI and Li metal are imaged prior to contact (Fig. 2d), on physical contact (Fig. 2e), electrochemical reduction (Fig. 2f), electrochemical oxidation (Fig. 2g) and after probe retraction (Fig. 2h,i). When a reducing bias is applied to LPS:0.5LiI, Li^+ ions are drawn out of the solid electrolyte (LPS:0.5LiI) and deposited on the Li probe. A void or pore forms in the solid electrolyte region in contact with the metallic probe after electrodeposition and is highlighted with a green box (Fig. 2f). This void is irreversible and remains after oxidation (Li^0 is stripped from probe) (Fig. 2g). The interphase void formation or loss of mass is evidence of edge chipping. Edge chipping, is a fracture mode, that most prominently occurs due to concentrated loads[56] or from a sharp contact[57]. While the probe can be considered a sharp

10
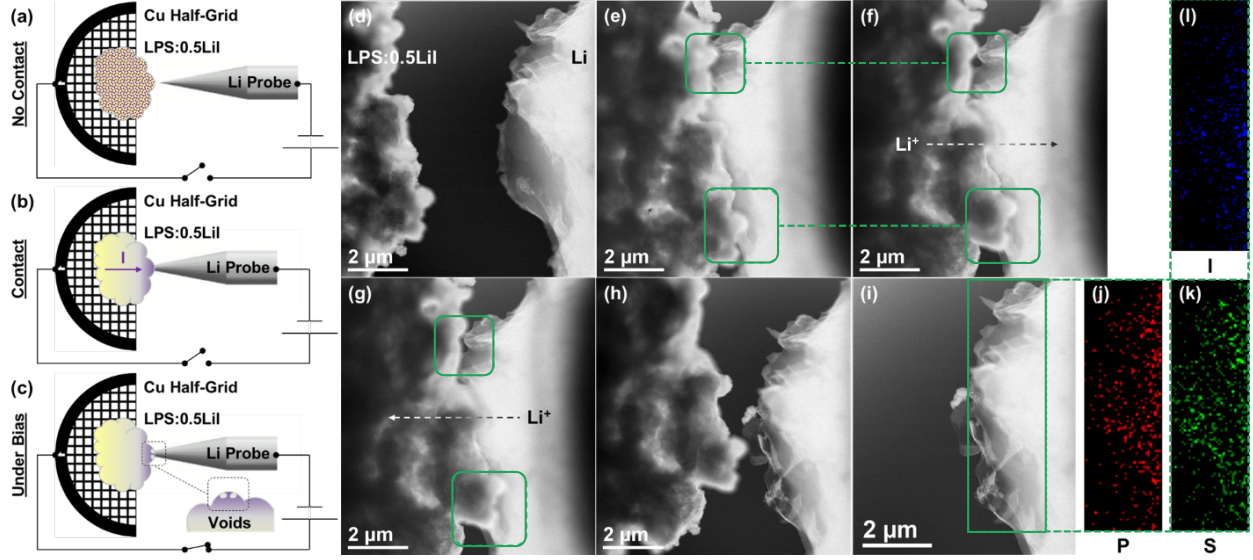
Figure 2: Interphase transformation tracked by *In Situ* TEM (a) Animation of the in-situ TEM Nanomanipulator holder highlighting the arrangement of Li and LPS:0.5LiI, (b) animation depicting the contact of Li and LPS:0.5LiI and resulting chemical processes (migration of iodine) within the TEM, (c) animation depicting the electrochemical processes (formation of voids) observed upon application of bias within the TEM, (d) HAADF STEM image of the Li probe and LPS:0.5LiI solid electrolyte prior to contact, (e) HAADF STEM image of the Li probe and LPS:0.5LiI upon contact, highlighting regions of interest for the purpose of this study, (f) HAADF STEM image of variations in the highlighted sections via appearance of voids along the Li/LPS:0.5LiI interface after plating of Li, (g) HAADF STEM image after the stripping of Li with the retention of formed voids during Li plating in the highlighted sections, (h) HAADF STEM image of the detached Li probe and LPS:0.5LiI after a Li plating/stripping cycle, (i) HAADF STEM image highlighting an area of interest on Li utilized for EDS mapping after Li plating/stripping experiments, and (j), (k), (l) phosphorus, sulfur and iodine EDS maps of the highlighted area in (i), respectively.

contact, there was no edge chipping observed upon initial contact (Fig. 2d). Pore formation and/or edge chipping only occured after electrochemical reduction of the solid electrolyte

11

(Fig. 2f). This early stage fracture mode, observed within the interphase, is likely due to chemo-mechanical driving forces[36]. Local stresses within a solid electrolyte can impact dissolution and deposition kinetics ($Li^0 \xrightarrow{dissolution} Li^+$) and ionic transport pathways[35;58] and can lead to local 'hot-spots' for ionic flux[3;59]. This ionic flux directionality is postulated to be equivalent to an ionic concentrated load at solid|solid interface and be the origin for the observed edge-chipping.

HAADF STEM images and EDS maps of the solid electrolyte after cycling shows a uniform distribution of iodine, phosphorous and sulfur across the entire imaged area (Fig. S5). After electrochemical plating (Fig. 2f) and stripping (Fig. 2g) of Li^0, the presence of iodine remains evident in the Li metal (Fig. 2l). Iodine diffusion to the solid electrolyte|lithium metal interface is observed under both equilibrium (quiescent) and electrochemical biasing conditions. Iodine diffusion occurs at the point-of-contact between the solid electrolyte and metallic lithium and readily diffuses into the bulk lithium (Fig. 2l). This indicates that iodine diffuses along the entire Li metal surface and is not restricted to the region of physical contact. Surface diffusion of iodine provides a uniform deposition surface for Li metal during cycling. A uniform interface reduces the cell impedance and results in a reversibly smooth overpotential response. The intimate contact afforded by an iodine rich interface between Li metal and the solid electrolyte can enable efficient ion transport through the interphase and lead to improved electrochemical performance.

In situ synchrotron X-ray tomography was carried out on all mentioned LPS-based materials to quantitatively assess the onset and growth of mechanical failure and observe subsurface material transformation pathways upon Li cycling. It should be noted that the sample pellets ($\sim$2 mm) were slightly larger than the field-of-view (FoV, 1.8 mm) of the tomogra-

phy setup, and consequently the imaged region is from the center of the pellet. Symmetric Li|SE|Li cells were assembled in the *in situ* cell[47] to observe plating and stripping behaviors at 0.5 and 1 mA cm^{-2} (Fig. 3a). The *in situ* cell shows a higher overpotential for Li plating and stripping, than the conventional coin cell due to the low applied pressure (≤ 0.5 MPa) (Fig. S6). All the cells were run at increasingly higher current densities until either the polarization reduced to zero, or the overpotential value exceeded the range of the potentiostat. The shorting of the *in situ* cell was confirmed by electrochemical impedance spectroscopy (Fig. S7). The sample porosity before electrochemical cycling, computed from the reconstructed 3D images range from 0.48 for A–LPS sample to ≈ 0.05 for LiI–AN sample (Fig. 3b). It should be noted that the resolution of the tomography technique employed is 0.7 μm. Pores smaller than this size are not resolved and hence may lead to an under-estimation of the porosity values. The charge to failure values for *in situ* experiments follow the trend A–LPS<LPS:0.5LiI<LiI–AT<LiI–AN (25, 35, 40 and 90 mC respectively). The outer bounds of the trends are consistent between the lab-scale experiments and the sychrotron experiments. However, the LPS:0.5LiI and LiI–AT show different trends, with the latter showing a slightly higher charge to failure for the synchrotron experiments. The variation between the samples is small (≈ 5 mC) and could arise from small differences in assembly in the *in situ* cell. All materials were stable during the course of the *in situ* experiment and did not show signatures of material degradation (Fig. S1). This allows for reliable interpretation of the data as electrochemistry driven material transformation rather than thermodynamics driven material degradation. X-ray tomography works primarily on the principle of absorption contrast, where the intensity of a beam traversing through the sample is attenuated according

to the Beer-Lambert law,

$$I = I_0 exp(-\mu(x)x) \tag{2}$$
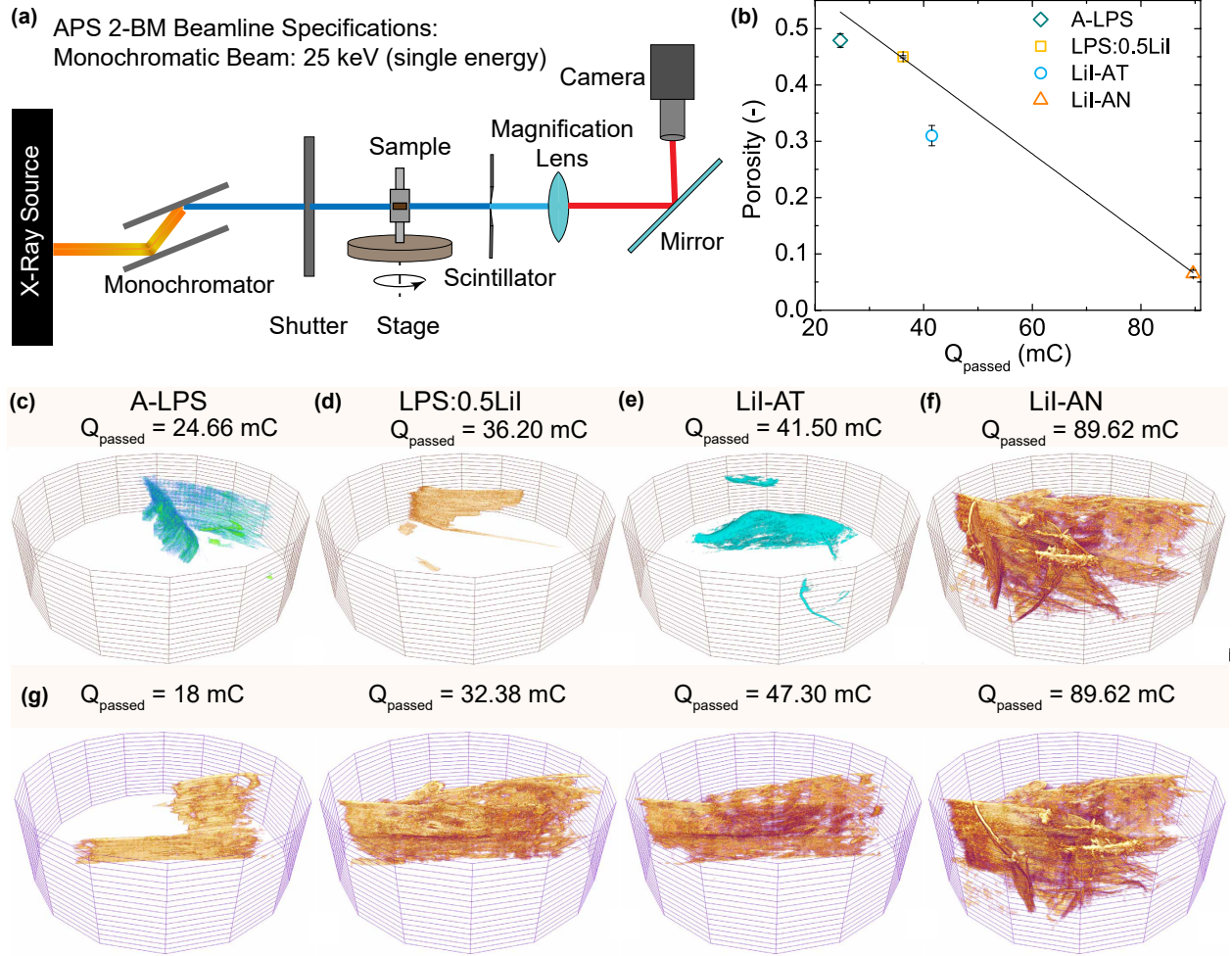
Figure 3: Failure onset and growth tracked by *in situ* synchrotron tomography. (a) Schematic diagram of the tomography setup used for *in situ* imaging of solid electrolytes (b) Correlation between the porosity measured from the tomography experiments and charge to failure. (c)-(f) 3D representation of cracks of the failed samples after cycling for A–LPS, LPS:0.5LiI, LiI–AT, and LiI–AN respectively. (g) Crack propagation through LiI–AN sample at various plating, stripping steps.

where, I is the intensity of the transmitted beam, I_0 is the incident beam intensity and

$\mu(x)$ is the absorption coefficient of the material. Denser materials characterized by high Z-elements (solid electrolyte) attenuate the X-rays more than low-Z elements (Li metal and/or air). This difference in attenuation allows for tracking individual material transformations during electrochemical cycling. Reconstructed images clearly show presence of distinct crack features in the 2D sections (Fig. S8). The fracture regions were segmented out from the raw reconstruction images for visualization (Fig. 3c-f). The segmentation was carried using consistent semi-automated procedures for all the samples. Due to the small feature size of the fracture event and segmentation methodology, the crack regions are generally over-estimated (rather than underestimated). However, since the segmentation protocol is consistent at all steps and across samples, comparisons can be made between them. The cracks are concentrated in one region of the pellet for A–LPS, LPS:0.5LiI and LiI–AT, while the crack is uniformly distributed in the LiI–AN samples. The fracture region grows toward regions with high porosity during symmetrical cycling which mimics a Griffith crack like mechanism[16]. The overall mechanical strength of the solid electrolyte in regions with high porosity will be low and be more susceptible to fracture. All solid electrolytes have some level of meso- and microstructure which is introduced during materials processing. Although it is ideal to have a low porosity material, the way the material is pressed in a pellet can lead to non-uniform pore sizes throughout the pellet. Regions with high porosity contribute to tortuous ion transport that can locally magnify the current density and electric fields. The latter effect may promote localized ionic flux capable of chipping the solid electrolyte interface.

The cracks were also segmented at the end of individual charging/discharging step to visualize the onset and growth mechanism of crack propagation of the sample (Fig. 3g, S9). Based on these images, it was found that all the materials showed two distinct failure modes

15

(Fig. 4a): (i) edge chipping failure of electrolyte section at electrode|electrolyte interface and (ii) vertical crack growth through sample thickness originating from the chipped electrolyte section. The fracture onset via edge chipping is likely do to directed ion transport (chemomechanics) in the interphase as seen with *in situ* TEM experiments (Fig. 2f). Interphase void generation leads to regions of high current density and stress concentration that can lead to fracture of the solid electrolyte at the interface. This mechanism is consistent over length scales and is effectively observed as the crack onset mechanism. *In situ* tomography corroborates microscopy observations and demonstrates initiation of edge chipping at the stripping electrode (Fig. 4b-c). Subsequently, from this region a lateral crack develops that grows through the thickness of the sample (Fig. 4d). Similar interface driven fracture was proposed previously for Na β-alumina solid electrolytes[60]. Surface irregularities were identified as potential stress concentration regions through which fracture can initiate. Metal flow through this surface-driven crack propagates the fracture through the thickness of the electrolyte leading to ultimate failure by shorting. Edge chipping failure mode is characterized by removal of material from a surface/edge section due to high stress concentrations and is widely observed in material shaping, tribology, anthropology and dentistry[61;62;63;64;65]. The edge chipping was observed in all thioposphate electrolytes (independent of microstructure) and is likely chemo-mechanically driven. The through-plane or vertical fracture is a result of the solid electrolyte microstructure.

All samples fractured in a similar way despite differences in microstructure and interphase properties. These results indicate that while halide doping can kinetically stabilize the Li metal-LPS interface, the eventual failure mechanism for all the samples is identical. As this is a symmetric cell, these features are found on both electrodes and the short happens
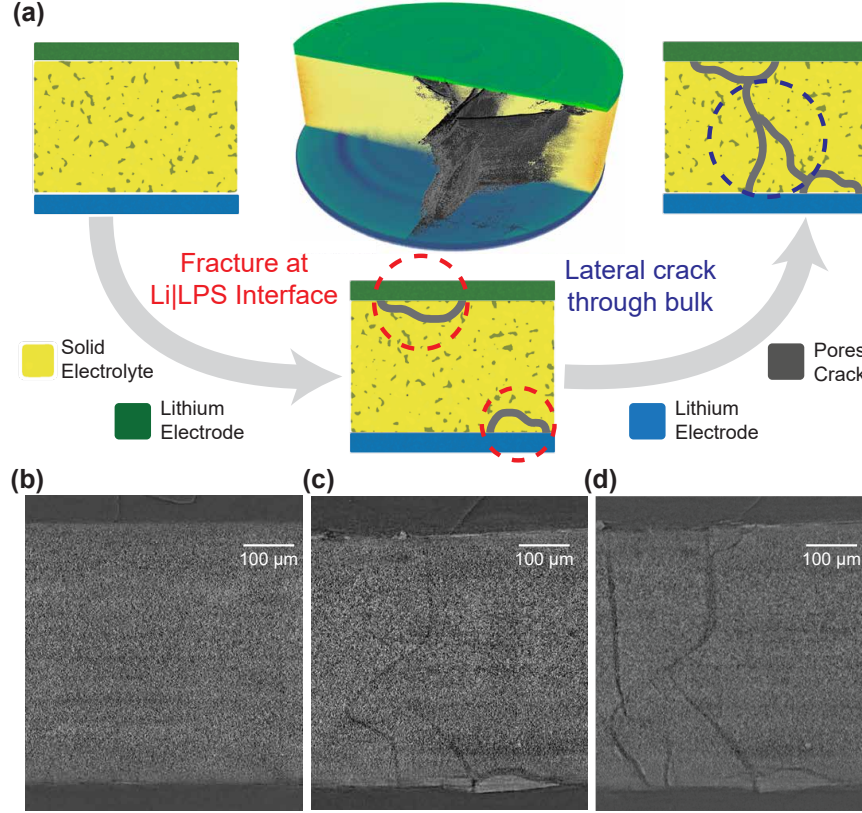
Figure 4: Failure mechanism in LPS. (a) Schematic diagram showcasing the failure onset and growth mechanism in LPS solid electrolytes. Pristine LPS pellet shows a heterogeneous distribution of porosity (darker regions). Mechanical failure initiates by chipping failure of an electrolyte block at the electrode|electrolyte interface. The chipping mechanism is initiated by active electrochemical oxidation and reduction and is not observed on passive contact. Further cycling leads to lateral crack growth from the regions showing chipping failure through the thickness of the electrolyte. Sectional reconstruction images of LiI–AN material clearly show these distince phenomenological mechanism: (b) pristine, (c) chipping failure and (d) lateral crack growth.

when the propagating lateral cracks merge within the bulk. It should be noted that Li presence is possible in the crack features observed by tomography due to filament growth. Li penetration in to the crack features exposes additional SE surface to Li metal increasing the Li|LPS interfacial area. Solid electrolyte in contact with Li within these crack features can

undergo interphase formation and related chemo-mechanical transformations as evidenced from TEM measurements. Additional interphase formation within the cracks can lead to an accelerated failure. Combining tomography and TEM provides unique collective insight into the failure onset mechanism in LPS electrolytes over several length scales.

In situ transmission electron microscopy revealed that iodine rapidly diffuse to the solid electrolyte|Li metal interface. This will result in a compositional gradient in the solid electrolyte. Prior work demonstrated that halide doping led to materials with lower Young's modulus and less elasticity due to a larger free volume[66,37]. Thus, iodine diffusion to the interface will lead to non-uniform mechanical properties throughout the solid electrolyte. Solid electrolytes doped with a halogen will have electrode|electrolyte interfaces with lower Young's modulus compared to the bulk. These interfaces will be more compliant toward the plating and stripping stress and may explain the higher critical current density and charge-to-failure for the halogen-doped solid electrolytes. Iodine doping and improved packing density of annealed samples result in higher performance metrics (CCD, $Q_{failure}$). While the failure onset mechanism is identical for all mentioned LPS materials, the extent of crack propagation (density of cracks in the bulk) varies significantly between the different materials. This suggests that the lateral crack growth is governed by differences in bulk pellet microstructure.

Solid electrolyte microstructure heteogenity can result in non-uniform mechanical stress. Regions with higher porosity have lower yield strength which results in stress accumulation. Thus, lateral crack growth tends to nucleate at porous regions (Fig. S9). Microstructure variability can be quantitatively assessed with a porosity factor (Fig. 5a-b). Porosity factor is defined as the variation in local porosity compared to the mean porosity:
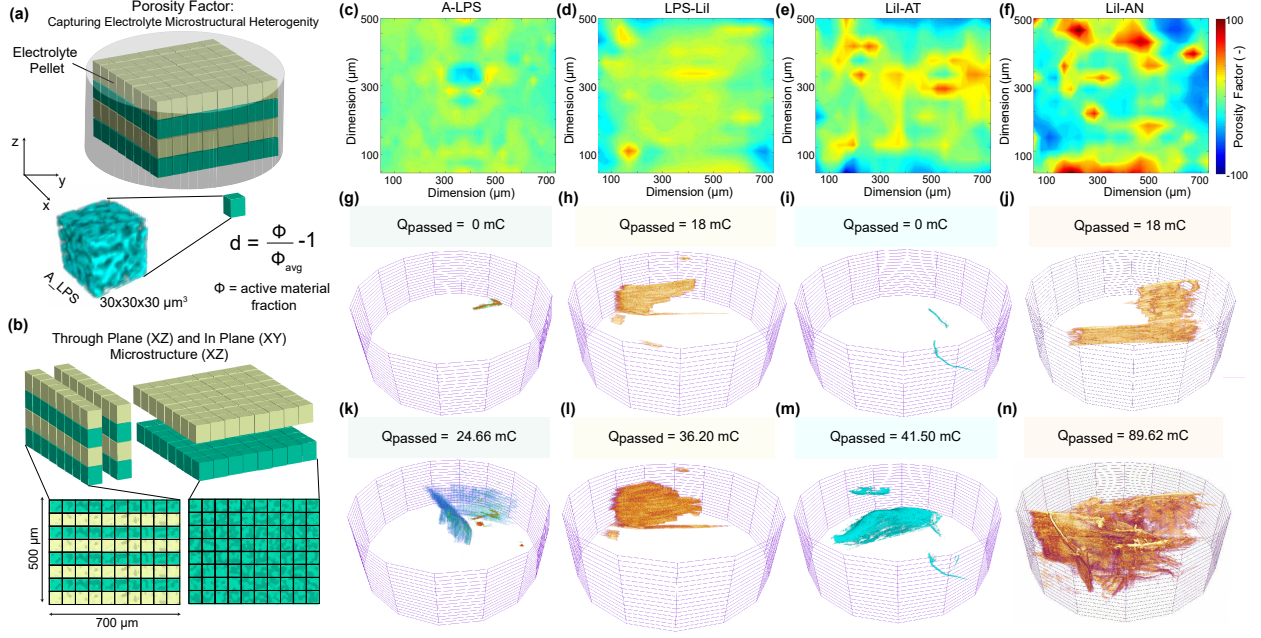
Figure 5: Assessing microstructural heterogeneity in solid electrolytes by porosity factor. (a) Electrolyte pellet is discretized into uniform sub-volumes of 30x30x30 μm^3 dimension. (b) Porosity factor is defined as the ratio of local porosity identified for the 30x30x30 μm^3 sub-volume to the average porosity of the pellet. Microstructure of a representative sub-volume of A–LPS pellet is shown. (c) Porosity maps are calculated across two normal planes in the electrolyte defined as through plane and in-plane directions. In-plane section are normal to the applied electric field and represent the horizontal cross section of the pellet. Through plane is parallel to the applied electric field and represents the vertical cross section of the pellet. Porosity factor variation in through-plane direction for A–LPS, LPS:0.5LiI, LiI–AT, LiI–AN (c)-(f). Initial crack formation in samples for A–LPS, LPS:0.5LiI, LiI–AT, LiI–AN (g)-(j). A–LPS and LiI-AT pristine pellets showed regions with microstructure distinct from the average microstructure. Hence, those morphologies are visualized. 3D representation of cracks of the failed samples after cycling for A–LPS, LPS:0.5LiI, LiI–AT, and LiI–AN respectively (k)-(n).

$$d = \frac{\Phi}{\Phi_0} - 1, \tag{3}$$

where d is the porosity factor, Φ is the local porosity and Φ_0 is the mean porosity calculated on a binarized dataset. Porosity maps are calculated across two normal planes in the electrolyte defined as through plane and in-plane directions (Fig. 5b). In-plane section are normal to the applied electric field and represent the horizontal cross section of the pellet. Through plane is parallel to the applied electric field and represents the vertical cross section of the pellet. Mapping the porosity factor along the through-plane direction we clearly observe local regions with inhomogeneous microstructure compared to the average microstructure (Fig. 5c-f). A–LPS shows a more homogeneous distribution of porosity factor compared to LiI–AN which has a highly inhomogeneous distribution through the section. Porosity factors mapped here are local measurements that reflect the microstructural features at specific locations in the sample. It should be noted that the porosity factor shown here is a relative change in the local microstructural property compared to a mean microstructural property. Statistically, the absolute variation of local porosity should be identical because all pellets are processed in a similar way. Normalizing this value by the mean porosity gives an insight into the degree of structural heterogeneity. For A–LPS sample, with a mean porosity of 0.48, a local variation of 0.02-0.03 does not deviate significantly from the average microstructure. However, for LiI–AN, a local variation of 0.02-0.03 is comparable to its mean porosity (0.05) which is characterized as high structural heterogeneity (Fig. 5c-f). Statistical analysis of porosity factor was carried out on 40 distinct $\approx$750x500x30 μm^3 electrolyte cross-sections (Fig. S10). Statistical assessment of the porosity factor across this dataset

shows consistent results with A–LPS showing a homogeneous, narrow distribution of porosity factor while LiI–AN shows a more heterogeneous, wide distribution of porosity factors. This is further verified by in-plane assessment of porosity factor across different sub-volumes sizes for the raw gray-scale dataset to remove errors from the binarization process (Fig. S11, S12). These studies also show consistent results with LiI–AN having the most heterogeneous microstructure (compared to its mean value). The influence of porosity factor distribution is observed on the crack formation within the electrolytes (Fig. 5g-n). A–LPS, which showed a relatively homogeneous porosity factor, shows focused crack formation in the vicinity of a microstructural feature present in the pristine sample (Fig. 5g,k). In comparison, LiI–AN, which shows highly heterogeneous porosity factor distribution, shows extensive crack propagation through the entire bulk of the sample with no apparent focused crack growth (Fig. 5j,n). LPS:0.5LiI and LiI–AT show similar behavior in terms of crack formation and porosity factor distribution. Crack growth through the sample is dictated by the mechanics of the bulk electrolyte. The microstructural variation observed in the pellets indicate that cracks will preferentially grow through the regions with higher porosity (lower porosity factor) due to the reduced local mechanical properties. Additionally, higher porosity increases the local tortuosity in the region leading to an enhanced current density and electric field in the vicinity. These effects lead to crack formation in regions with high microstructural heterogeneity. Controlling porosity and pore distribution within the pellet will be important to tailor solid electrolytes for high rate capability.

Current focusing, can occur because of solid electrolyte microstructure heterogenity or constriction effects. Constriction effects can lead to polarization and is often due to distant active microcontacts (irregular contact) which leads to lower contact surface area, local re-
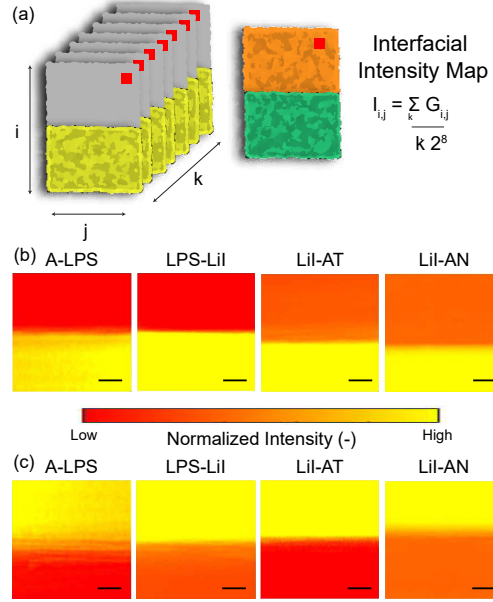
Figure 6: Interfacial intensity map at the solid|solid interface. (a) Schematic diagram explaining the measurement of intensity maps. Raw grayscale intensity is traced a 150x150 μm^2 section over at least 500 μm depth. This is normalized to the depth and the maximum theoretical intensity of an 8-bit image. The resultant image provides insight into the density variation and presence of pores/voids within the imaged section. Intensity map for the top Li|SE interface are shown in (b) while for the bottom SE|Li interface are shown in (c). All the scale bars in the figure are 30 μm.

gions with higher current densities, and high stress distributions[67;68]. These non-conformal regions can accelerate material transformations leading to failure. To effectively rule out that sample contact had a role in current focusing, we created interfacial intensity maps (Fig. 6). Interfacial intensity maps qualitatively indicate the degree of interfacial contact and are generated by normalizing the gray scale intensity of a 150x150 μm^2 section at both Li|SE interfaces over at least a 500 μm thickness for the pristine cell (Fig. 6a). Regions with high normalized intensity signify high attenuation materials (solid electrolyte) while lower intensity materials signify transparent regions (air/voids). Relative densities of the solid

electrolytes are clearly discernible within the interface maps, but no significant differences are seen at the interfaces across all four samples (Fig. 6b-c, S13). The identification of heterogeneity at the interface is limited by the size of the voids, resolution of the technique and the contrast available between Li and void regions. For the given experimental conditions, no discernible differences are observed in the average interface conformation for the four samples. This indicates that the crack formation mechanism are driven by inherent material microstructural heterogeneity and not due to variations in cell assembly (contact between electrode and electrolyte).

Resolving lithium filaments in the bulk solid electrolyte is challenge because both voids and lithium have low contrast and will be transparant. Thus, instead of directly tracking lithium filament within the bulk electrolyte, we indirectly monitor it via tracking the total transparant region. An increase in the transparent region will occur either via an increase in the void region (via fracture growth) or by the presence of lithium metal in the bulk solid electrolyte. X-ray transparent region volume within the solid electrolyte bulk is tracked during cycling to assess the presence of electrochemically active material within the LiI–AN solid electrolyte (Fig. 7a) and A-LPS,LPS:0.5LiI, LiI-AT (Fig. S14). The X-ray transparent region volume grows at crack onset and oscillates on subsequent cycles (Fig. 7c, S14) prior to failure by shorting for all the samples studied. It should be noted that the absolute crack volumes are most likely over-estimated due to segmentation challenges. However, the trends between individual steps can be compared as the same segmentation protocols were employed across all the samples. The X-ray transparent regions are areas showing lower absorption than the surrounding electrolyte material which can be pores, cracks or Li metal all of which have low absorption coefficients. The volume modulation of the X-

ray transparent region can be presence of electrochemically active material (Li) within the cracks (Fig. 7b). Presence of metal in crack is consistent with the failure mechanisms proposed for other solid electrolytes[60]. During the plating cycle Li can be deposited in the crack onto a filament growth or deposit in an isolated form. On stripping, if this material is electrochemically accessible it will be oxidized and shuttled to the other electrode. This creates a mismatch in the crack propagating stress (tensile) and the restoring stress offered by the pellet (compressive). If the stress exerted by the Li filament inside the crack exceeds the yield strength of the electrolyte material, fracture will occur. Li filament growth into the solid electrolyte also increases the Li|LPS interfacial area. The regions with new interfacial contact between Li and solid electrolyte undergo interphase formation and chemo-mechanical transformations like void formations, iodine migration, and stress gradient formation as evidenced from the *in situ* TEM measurements.

A validation of Li filament growth within the imaged cracks is carried out by assessing the cycled capacity from the individual electrodes of the symmetric cell at each step (Fig. 7b, S14). The cycled capacities are estimated from the change in thickness of the electrode between successive plating/stripping steps. The thicknesses of the electrodes are averaged over 15 spatial locations across the sample, assuming planar plating and stripping. While this assumption is not very accurate, it provides some information regarding the depth of discharge from individual electrodes. We clearly observe an unequal amount of plated and stripped charge for the individual electrode, especially for later steps. The excess charge can be thought to reside in the X-ray transparent regions imaged and thus account for the modulation of the crack volumes observed. Non-uniform crack formation and subsequent fatigue loading by cycling of active material through the cracks can lead to fracture of the
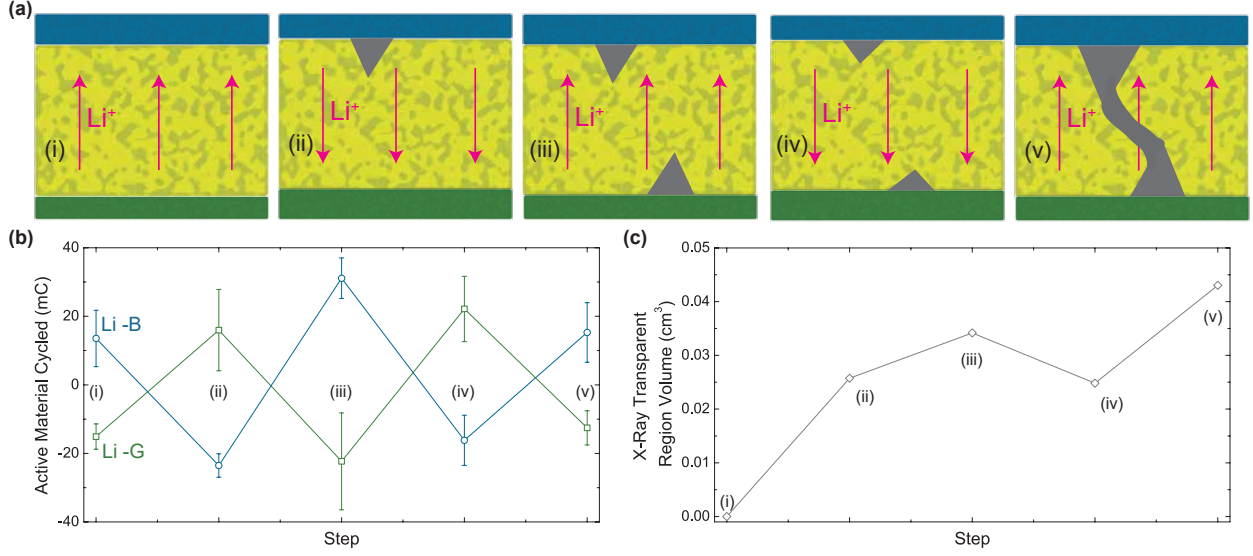
Figure 7: Crack Volume Modulation on Cycling in LiI–AN. (a) Schematic diagram representing the variation in imaged crack volume upon cycling. (b) Difference in average electrode thickness of the plating and stripping electrode as a function of cycle steps. (c) Absolute crack volumes measured as a function of cycle steps.

solid electrolyte.

3   Conclusions

In summary, the effect of interfacial chemistry and microstructure on the mechanical failure of LPS-based solid electrolytes is investigated using advanced multimodal characterization techniques. Kinetically stable interphase and microstructural control is engineered by iodine doping, and milling and annealing respectively. The annealed samples with iodine doping show the highest room temperature conductivity of 2.4×10^{-3} S cm^{-1} and critical current density of 4 mA cm^{-2}. *In situ* TEM results show iodine migration to the Li metal surface and void formation at the LPS interface on electrochemical cycling. Void formation only occurs

upon electrochemically cycling which suggest that the transformation is chemo-mechanically driven via local 'hot spots' in ion flux. Iodine migration to the Li metal surface affords nm-scale intimate contact with Li metal resulting in improved electrochemical performance of the LiI containing materials. Void formation at the LPS interface is an inherent material response to electrochemical cycling and is not observed on passive contact. Material transformations during cycling are evaluated using *in situ* synchrotron X-ray tomography. A consistent failure mechanism across all materials is identified by tracking evolution of the crack features in the *in situ* tomography data. Mechanical failure is initiated with edge cracking at the interface and subsequent lateral crack growth through the surface. The onset of failure at the Li|LPS interface is consistent with the void formation observed in the TEM studies. Extent of crack propagation within the bulk solid electrolyte is assessed by tracking the porosity factor of solid electrolytes. Annealed sample shows large spatial microstructural heterogeneity leading to an extensive crack formation through the bulk dictated by the tortuous ion flux pathways and disparate local mechanical properties. Volume modulation of X-ray transparent region and non-symmetric depth of discharge on the two electrodes indicates Li filament growth and presence of active material in the crack features. Non-uniform crack formation and subsequent fatigue loading by cycling of active material through the cracks can lead to fracture of the solid electrolyte. *In situ* TEM and XRT corroborates the failure mechanism across cascading length scales. Multimodal characterization offers a unique insight into failure mechanisms of solid-state batteries.

4 Experimental Methods

4.1 Sample Preparation

Synthesis of Li$_3$PS$_4$ (A-LPS)

Anhydrous lithium sulfide (Li2S) (Aldrich, 99.98%) and anhydrous phosphorus pentasulfide (P$_2$S$_5$) (Sigma-Aldrich, 99%) first form a mixture (2.0 g total) containing a molar ratio of Li$_2$S:P$_2$S$_5$ = 3:1. This mixture was ground by hand in an agate mortar/pestle for 5 minutes and then transferred to a 45 mL zirconium oxide (ZrO$_2$) ball-mill pot along with 32 g of ZrO$_2$ balls (5 mm diameter). The mixture was ball-milled for 40 hours using a planetary ball mill (Pulverisette 7, Fritsch). Afterward, the yellow lithium thiophosphate (Li$_3$PS$_4$-LPS) powder was collected.

Synthesis of Li$_3$PS$_4$:0.5LiI (LPS:0.5LiI)

Anhydrous lithium iodide (LiI) beads (Aldrich, 99.999%) were added to an agate mortar/pestle and pulverized. Then, LiI was moved to a new mortar along with anhydrous Li$_2$S and anhydrous P$_2$S$_5$ to form a mixture (2.0 g total) containing a molar ratio of Li$_2$S:P$_2$S$_5$: LiI = 3:1:1. This mixture was ground for 5 minutes and then transferred to a 45 mL ZrO$_2$ ball-mill pot along with 32 g of ZrO$_2$ balls (5 mm diameter). The mixture was ball-milled for 40 hours using a planetary ball mill (Pulverisette 7, Fritsch). Each cycle consisted of spinning the pot for 1 h at 550 rpm and then resting the pot for 5 min. Afterward, the LPS·0.5LiI (light yellow) powder was collected.

Synthesis of attrition milled LPS:0.5LiI (LiI-AT)

2 g of LPS:0.5LiI was transferred to a 45 mL ZrO_2 ball-mill pot along with 43 g of ZrO_2 balls (1 mm diameter). 6 g of dried heptane was added to the pot before sealing. The mixture was ball-milled for 12 hours using a planetary ball mill (Pulverisette 7, Fritsch). Each cycle consisted of spinning the pot for 1 h at 200 rpm and then resting the pot for 5 min. The white powder was collected and rinsed with 6 g of dried heptane and heated on a hot-plate while stirring at 100 °C for 3 hours. Afterward, the LiI-AT (white color) powder was collected.

Synthesis of annealed LPS:0.5LiI (LiI-AN)

2 g of LiI-AT was placed into a stainless steel can on a hot-plate. The mixture was heated at 185 °C for 3 hours while stirring every 20 minutes. Afterward, the LiI-AN (light-grey color) powder was collected.

4.2   Cell Assembly and Electrochemistry

Fabrication of impedance measurement cells

100 mg of solid electrolyte powder was added to the hole in a Macor ring (SA = 1.0 cm^2) and cold-pressed between two steel pistons into a pellet under 4 tons of pressure for 5 min. Then, carbon-coated aluminum foil (MTI corp.) disks were placed against both sides of the pellet and the stack was pressed again under 3 tons for about 1 min. After removing the stack from the press, the pistons were anchored in place by a cell top and bottom, held together by insulated bolts. The bolts were tightened to 2 N·m, which provides a stack pressure of about 88 MPa. Finally, the cell was sealed in an argon-filled container and placed into a

temperature-controlled oven. Electrochemical impedance spectroscopy was performed using a Bio-logic VMP3 Potentiostat, with a frequency range from 100 mHz to 1 MHz and a potential amplitude of 10 mV. The electrolyte resistance was determined from the EIS plots by extrapolating the low-frequency, linear section of the curves down to the x-axis.

Fabrication of Li/Solid Electrolyte/Li symmetric cells

For LPS:0.5LiI measurements, 100 mg of solid electrolyte was added to the hole in a Macor ring (SA = 1.0 cm^2) and cold-pressed between two steel pistons under 4 tons of pressure for 5 min to form a pellet. Then a thick lithium (Li) disk (99.8%, Honjo Metal) of 10 mm diameter was polished with a toothbrush, punched from the flattened Li using a knife punch and placed on both sides of the pellet. The final thickness of the Li foil is 150 μm. Stainless-steel pistons were pressed against the Li to form a stack, which was then sandwiched between cell top and bottom. Finally, insulated bolts were used to compress the cell to 29 MPa before placing the cell into an argon-filled container, which was then moved from the glove box to an oven for electrochemical testing.

Critical Current Density (CCD) test

Li metal was plated and stripped at step-wise-increased current densities using a Bio-logic VMP3 Potentiostat. At 60 °C, the current density was increased in a stepwise manner from 0.1 mA/cm2 to 4.0 mA/cm2 in 0.25 mA/cm2 increments. Each current was applied using 1-hour half-cycles for 2 cycles. The CCD was ascribed to the current at which a sharp drop in potential was witnessed mid-half-cycle.

Fabrication of Synchrotron Cells

For synchrotron experiments, 3 mm electrolyte pellets were made by compressing the samples at 4 tons/cm^2 pressure. The samples were transferred to the beamline in Argon atmosphere sealed containers. Symmetric Li|Li cells were assembled in the *in situ* cell inside an Argon atmosphere glovebox (< 0.1 ppm O$_2$ and H$_2$O) and sealed. The *in situ* cell was mounted on the sample stage at the end station. Electronic impedance spectroscopy was carried out before and after the complete testing of the symmetric cell between 1 MHz and 100 mHz with an amplitude of 50 mV. Plating and stripping experiments were carried out at current densities of 0.04 - 1.2 mA cm^{-2} for 30 minutes duration. A cut-off voltage of 10 V was kept for the tests. If the polarization exceeded this value, the current density was moved to the next step.

4.3   Tomography Studies

Synchrotron X-ray tomography studies were carried out at the 2-BM beamline of the Advanced Photon Source (Fig. 3a). Filtered monochromatic X-rays of 25 keV were incident on the sample. 1500 projections were taken evenly during a 180 ° sample rotation with 100 ms exposure time for each projection. FLIR Oryx ORX-10G-51S5M camera was used with a 2x magnification objective lens. The resultant voxel size was ≈0.7 μm and a field of view of 1.4 x 0.8 mm^2. With these experimental conditions, a single tomography scan took approximately 7-10 minutes of acquisition time. The tomography scans were taken for the pristine and the failed sample. Additionally, tomography scans were obtained at the end of each plating and stripping cycle.

4.4 Image Reconstruction, Analysis and Quantification

Tomopy software was used for reconstruction of the raw data[69] using Gridrec algorithm[70]. Wavelet-Fourier ring filter removal[71] and Paganin phase retrieval[72] methods were applied for raw image manipulation. Subsequent image processing was carried out using Image J[73] and MATLAB. Binarization of all the samples were carried out using identical thresholding routines available in ImageJ. The thresholding protocols were kept identical across all the analysed tomography scans to reduce variability in the results. Subvolume optimization was carried out to estimate geometric parameters of the system. Pore size distribution[74] plugin was used to estimate the porosity of the samples. The details of the method used to describe porosity and pore size distribution is reported previously[50]. Identification cracks from the binarized data was carried out by filtering pores smaller than a specified threshold volume and subsequently by visual analysis. All quantification routines were developed and implemented in MATLAB.

4.5 Microscopy Imaging Methods

Scanning Electron Microscopy (SEM)/Energy Dispersive X-ray Spectroscopy (EDS)
SEM images were collected using a JEOL 7800 FLV microscope outfitted with an Oxford EDS system, operated at 5-20 kV for all samples. All samples were loaded into an air-free SEM holder (JEOL) within an Argon atmosphere glove box (< 0.1 ppm O2 and H2O) and transported directly to the SEM where they were analyzed under vacuum.

Transmission Electron Microscopy (TEM)/Energy Dispersive X-ray Spectroscopy (EDS) HAADF

STEM images were collected using a JEOL JEM-F200 microscope operated at 200 kV. Dual silicon-drift detector EDS systems with a large solid angle (100 mm2) were utilized for enhanced microanalysis of all samples via ex-situ and in-situ analysis modes. Further details on *ex situ* and *in situ* TEM measurements are included in the supporting information.

Acknowledgements

Author Contributions

K.B.H. conceived the concept and idea. N.S. and T.S.A. synthesized the material and performed electrochemical measurements. M.B.D., N.S., T.S.A., K.B.H. and P.S. performed the synchrotron imaging experiments. M.D. completed the image processing and analysis from the synchrotron experiments. N.S., T.S.A., J.S.P., and E.A.S. did the TEM measurements. K.B.H. and M.B.D. wrote the manuscript. All authors contributed to revision of the manuscript.

Competing Interests

The authors declare no competing interests.

References

[1] Xin-Bing Cheng, Chen-Zi Zhao, Yu-Xing Yao, He Liu, and Qiang Zhang. Recent Advances in Energy Chemistry between Solid-State Electrolyte and Safe Lithium-Metal Anodes. <u>Chem</u>, 0(0):74–96, 2019.

[2] Kelsey B. Hatzell, Xi Chelsea Chen, Corie Cobb, Neil P Dasgupta, Marm B. Dixit, Lauren E Marbella, Matthew T. McDowell, Partha Mukherjee, Ankit Verma, Venkatasubramanian Viswanathan, Andrew Westover, and Wolfgang G. Zeier. Challenges in lithium metal anodes for solid state batteries. <u>ACS Energy Letters</u>, 5:922–934, 2020.

[3] Christian Masquelier. Solid electrolytes: Lithium ions on the fast track. <u>Nature Publishing Group</u>, 10(9):649–650, 2011.

[4] Jonathan Lau, Ryan H. DeBlock, Danielle M. Butts, David S. Ashby, Christopher S. Choi, and Bruce S. Dunn. Sulfide Solid Electrolytes for Lithium Battery Applications. <u>Advanced Energy Materials</u>, 8(27):1–24, 2018.

[5] Satoshi Ujiie, Akitoshi Hayashi, and Masahiro Tatsumisago. Preparation and ionic conductivity of (100-x)(0.8Li2S·0. 2P2S5)·xLiI glass-ceramic electrolytes. <u>Journal of Solid State Electrochemistry</u>, 17(3):675–680, 2013.

[6] Raimund Koerver, Wenbo Zhang, Lea De Biasi, Simon Schweidler, Aleksandr O. Kondrakov, Stefan Kolling, Torsten Brezesinski, Pascal Hartmann, Wolfgang G. Zeier, and Jürgen Janek. Chemo-mechanical expansion of lithium electrode materials-on the route to mechanically optimized all-solid-state batteries. <u>Energy and Environmental Science</u>, 11(8):2142–2158, 2018.

[7] Pascal Hartmann, Thomas Leichtweiss, Martin R Busche, Meike Schneider, Marisa Reich, Joachim Sann, Philipp Adelhelm, and Ju¨rgen Janek. Degradation of nasicon-type materials in contact with lithium metal: formation of mixed conducting interphases (mci) on solid electrolytes. The Journal of Physical Chemistry C, 117(41):21064–21074, 2013.

[8] Sebastian Wenzel, Simon Randau, Thomas Leichtweiß, Dominik A. Weber, Joachim Sann, Wolfgang G. Zeier, and Jürgen Janek. Direct Observation of the Interfacial Instability of the Fast Ionic Conductor Li10GeP2S12 at the Lithium Metal Anode. Chemistry of Materials, 28(7):2400–2407, 2016.

[9] Sebastian Wenzel, Dominik A. Weber, Thomas Leichtweiss, Martin R. Busche, Joachim Sann, and Jürgen Janek. Interphase formation and degradation of charge transfer kinetics between a lithium metal anode and highly crystalline Li7P3S11 solid electrolyte. Solid State Ionics, 286:24–33, 2016.

[10] Cheng Ma, Yongqiang Cheng, Kuibo Yin, Jian Luo, Asma Shara, Je Sakamoto, and Juchuan Li. Interfacial Stability of Li Metal − Solid Electrolyte Elucidated via in Situ Electron Microscopy. 2016.

[11] Fudong Han, Yizhou Zhu, Xingfeng He, Yifei Mo, and Chunsheng Wang. Electrochemical stability of li10gep2s12 and li7la3zr2o12 solid electrolytes. Advanced Energy Materials, 6(8):1501590, 2016.

[12] Sebastian Wenzel, Simon Randau, Thomas Leichtweiß, Dominik A. Weber, Joachim Sann, Wolfgang G. Zeier, and Jürgen Janek. Direct Observation of the Interfacial Insta-

bility of the Fast Ionic Conductor Li10GeP2S12at the Lithium Metal Anode. <u>Chemistry of Materials</u>, 28(7):2400–2407, 2016.

[13] Valentin Wenzel, Hermann Nirschl, and Dorit Nötzel. Challenges in Lithium-Ion-Battery Slurry Preparation and Potential of Modifying Electrode Structures by Different Mixing Processes. <u>Energy Technology</u>, 3(7):692–698, 2015.

[14] Jared Tippens, John C. Miers, Arman Afshar, John A. Lewis, Francisco Javier Quintero Cortes, Haipeng Qiao, Thomas S. Marchese, Claudio V. Di Leo, Christopher Saldana, and Matthew T. McDowell. Visualizing Chemomechanical Degradation of a Solid-State Battery Electrolyte. <u>ACS Energy Letters</u>, 4(6):1475–1483, 2019.

[15] Sebastian Wenzel, Thomas Leichtweiss, Dominik Krüger, Joachim Sann, and Jürgen Janek. Interphase formation on lithium solid electrolytes - An in situ approach to study interfacial reactions by photoelectron spectroscopy. <u>Solid State Ionics</u>, 278:98–105, 2015.

[16] Lukas Porz, Tushar Swamy, Brian W Sheldon, Daniel Rettenwander, Till Frömling, Henry L Thaman, Stefan Berendts, Reinhard Uecker, W Craig Carter, and Yet-Ming Chiang. Mechanism of Lithium Metal Penetration Through Inorganic Solid Electrolytes. <u>Advanced Energy Materials</u>, 7(20):1701003, 2017.

[17] Asma Sharafi, Harry M Meyer, Jagjit Nanda, Jeff Wolfenstine, and Jeff Sakamoto. Characterizing the Li–Li7La3Zr2O12 Interface Stability and Kinetics as a Function of Temperature and Current Density. <u>Journal of Power Sources</u>, 302:135–139, 2016.

[18] Eric Kazyak, Regina Garcia-Mendez, William S LePage, Asma Sharafi, Andrew L Davis, Adrian J Sanchez, Kuan-Hung Chen, Catherine Haslam, Jeff Sakamoto, and Neil P

Dasgupta. Li penetration in ceramic solid electrolytes: operando microscopy analysis of morphology, propagation, and reversibility. Matter, 2020.

[19] Fudong Han, Jie Yue, Xiangyang Zhu, and Chunsheng Wang. Suppressing Li Dendrite Formation in Li 2 S-P 2 S 5 Solid Electrolyte by LiI Incorporation. Advanced Energy Materials, 8(18):6–11, 2018.

[20] Syed Atif Pervez, Musa Ali Cambaz, Venkataraman Thangadurai, and Maximilian Fichtner. Interface in Solid-State Lithium Battery: Challenges, Progress, and Outlook. ACS Applied Materials and Interfaces, 11:22029–22050, 2019.

[21] Lin Xu, Shun Tang, Yu Cheng, Kangyan Wang, Jiyuan Liang, Cui Liu, Yuan-Cheng Cao, Feng Wei, and Liqiang Mai. Interfaces in Solid-State Lithium Batteries. Joule, 2:1–25, 2018.

[22] Jan Van Den Broek, Semih Afyon, and Jennifer L M Rupp. Interface-Engineered All-Solid-State Li-Ion Batteries Based on Garnet-Type Fast Li + Conductors. pages 1–11, 2016.

[23] Yizhou Zhu, Xingfeng He, and Yifei Mo. Origin of Outstanding Stability in the Lithium Solid Electrolyte Materials: Insights from Thermodynamic Analyses Based on First-Principles Calculations. ACS Applied Materials and Interfaces, 7(42):23685–23693, 2015.

[24] Lingzi Sang, Kimberly L. Bassett, Fernando C. Castro, Matthias J. Young, Lin Chen, Richard T. Haasch, Jeffrey W. Elam, Vinayak P. Dravid, Ralph G. Nuzzo, and Andrew A. Gewirth. Understanding the Effect of Interlayers at the Thiophosphate Solid

Electrolyte/Lithium Interface for All-Solid-State Li Batteries. Chemistry of Materials, 30(24):8747–8756, 2018.

[25] Fudong Han, Yizhou Zhu, Xingfeng He, Yifei Mo, and Chunsheng Wang. Electrochemical Stability of Li 10 GeP 2 S 12 and Li 7 La 3 Zr 2 O 12 Solid Electrolytes. Advanced Energy Materials, 6:1501590, 2016.

[26] Parvin Adeli, J David Bazak, Kern Ho Park, Ivan Kochetkov, Ashfia Huq, Gillian R Goward, and Linda F Nazar. Boosting solid-state diffusivity and conductivity in lithium superionic argyrodites by halide substitution. Angewandte Chemie International Edition, 58(26):8681–8686, 2019.

[27] Shuo Wang, Yibo Zhang, Xue Zhang, Ting Liu, Yuan-Hua Lin, Yang Shen, Liangliang Li, and Ce-Wen Nan. High-conductivity argyrodite li6ps5cl solid electrolytes prepared via optimized sintering processes for all-solid-state lithium–sulfur batteries. ACS applied materials & interfaces, 10(49):42279–42285, 2018.

[28] Satoshi Ujiie, Toru Inagaki, Akitoshi Hayashi, and Masahiro Tatsumisago. Conductivity of 70Li2S·30P2S5 glasses and glass-ceramics added with lithium halides. Solid State Ionics, 263:57–61, 2014.

[29] Feixiang Wu, Jung Tae Lee, Naoki Nitta, Hyea Kim, Oleg Borodin, and Gleb Yushin. Lithium iodide as a promising electrolyte additive for lithium-sulfur batteries: Mechanisms of performance enhancement. Advanced Materials, 27(1):101–108, 2015.

[30] Satoshi Ujiie, Akitoshi Hayashi, and Masahiro Tatsumisago. Structure, ionic conductiv-

ity and electrochemical stability of Li 2S-P 2S 5-LiI glass and glass-ceramic electrolytes. Solid State Ionics, 211:42–45, 2012.

[31] Rene Mercier, Jean-Pierre Malugani, Bernard Fahys, and Guy Robert. Superionic Conduction in Li$_2$S–P$_2$S$_5$–LiI–Glasses. Solid State Ionics, 5:663–666, 1981.

[32] LIU Cai, WEN Zhao-Yin, and RUI Kun. High Ion Conductivity in Garnet-type F-doped Li$lt;inf$gt;7$lt;/inf$gt;La$lt;inf$gt;3$lt;/inf$gt;Zr$lt;inf$gt;2$lt;/inf$gt;O$lt;inf$gt;12$lt;/inf$gt;. Journal of Inorganic Materials, 30(9):995, 2015.

[33] Yao Lu, Xiaoyi Meng, J.A. Alonso, María T. Fernández-Díaz, and Chunwen Sun. Effects of Fluorine Doping on Structural and Electrochemical Properties of Li6.25Ga0.25La3Zr2O12 as Electrolytes for Solid-State Lithium Batteries. ACS Applied Materials & Interfaces, page acsami.8b17656, 2018.

[34] Jonathan M Larson, Eleanor Gillette, Kristen Burson, Yilin Wang, Sang Bok Lee, and Janice E Reutt-Robey. Pascalammetry with operando microbattery probes: Sensing high stress in solid-state batteries. Science advances, 4(6):eaas8927, 2018.

[35] Aashutosh Mistry and Partha P Mukherjee. Molar volume mismatch: A malefactor for irregular metallic electrodeposition with solid electrolytes. Journal of The Electrochemical Society, 167(8):082510, 2020.

[36] Chengyin Fu, Victor Venturi, Jinsoo Kim, Zeeshan Ahmad, Andrew W Ells, Venkatasubramanian Viswanathan, and Brett A Helms. Universal chemomechanical design rules for solid-ion conductors to prevent dendrite formation in lithium metal batteries. Nature Materials, pages 1–9, 2020.

Supplementary Information:

In situ Investigation of Interphase and Microstructure effects on chemo-mechanics of thiophosphate solid electrolytes

Marm Dixit[1,+], Nikhilendra Singh[2,+], James P. Horwath[3], Pavel Shevchenko[4], Eric A. Stach[3,5], Timothy S. Arthur[*2], and Kelsey Hatzell[*1,6,7]

[1]*Department of Mechanical Engineering, Vanderbilt University*

[2]*Toyota Research Institute of North America*

[3]*Department of Material Science and Engineering, University of Pennsylvania*

[4]*X-Ray Science Division, Argonne National Laboratory*

[5]*Laboratory for Research on the Structure of Matter, University of Pennsylvania*

[6]*Interdisciplinary Department of Material Science, Vanderbilt University*

[7]*Department of Chemical and Biomolecular Engineering, Vanderbilt University*

[+]*equal contribution*

[*]*corresponding author: kelsey.b.hatzell@vanderbilt.edu, tim.arthur@toyota.com*

S1 Additional TEM Methods

Specific to ex-situ TEM: All samples for ex-situ analysis were loaded onto 3 mm 300-mesh lacy carbon coated copper grids (Ted Pella) within an Argon atmosphere glove box (< 0.1 ppm O_2 and H_2O). The loading was carried out by directly scooping the grid through the sample material contained within a glass vial. As such, this was a dry-casting method and no solvents were utilized during the process at any time to prevent possible reactions between sample materials and solvents. The material cast and analyzed using this process was Li_3PS_4:0.5LiI. In addition to general imaging and elemental analysis, ex-situ TEM was utilized as a benchmark to establish the necessary microscope settings (e.g. probe size, beam current, spot size, exposure time, etc.) to successfully image and analyze the materials without damage from the beam itself. It should be noted that each material is expected to have different behavior under the beam and as such should be benchmarked prior to in-situ TEM analysis efforts to ensure an optimized setup. Below, we provide a description of how the ex-situ holder (JEOL single-tilt) was setup for the experiments highlighted in this manuscript:

The holder was brought into the glove box using standard protocols and the holder tip was disassembled within the glove box to load a designated sample material. Specific tools for the holder were also brought into the glove box to ensure damage-free disassembly/assembly of the holder.

For all experiments, Li_3PS_4:0.5LiI material was loaded onto the grid using the procedure described above. The material loaded grid was then assembled into the holder component. The reassembled holder was now secured for air-free transfer from the glove box by using a

customized air-free holder cap. Once secure with this cap, the holder was removed from the glove box using standard protocols and immediately moved to the TEM for loading.

The holder was loaded into the TEM while the air-lock for the TEM holder vented either nitrogen or argon gas to ensure air-free entry of the holder into the TEM. The custom air-free holder cap was removed from the holder at the TEM point of entry immediately prior to loading the holder into the TEM and pumping it down instantly to minimize sample exposure to air during this process. The total time that the sample was exposed to air was on the order of 5 to 10 seconds.

Specific to in-situ TEM: All sample analysis was carried out using a Biasing Nanomanipulator Holder designed by Hummingbird Scientific. The holder assembly was carried out within an Argon atmosphere glove box (< 0.1 ppm O2 and H2O). This in-situ holder utilized a 3mm 300-mesh lacy carbon coated copper half-grid (Ted Pella) and a tungsten (W) scanning tunneling microscopy (STM) probe (Bruker). The biasing capability of the in-situ holder allowed for the application and observation of a current and/or voltage between the half-grid and STM probe. The movable STM probe could be brought into contact with the half-grid to complete a circuit and conduct electrochemistry experiments within the TEM. Below, we provide a description of how the in-situ holder was setup for the experiments highlighted in this manuscript:

The holder was brought into the glove box using standard protocols and the holder tip was disassembled within the glove box to separate components for the half-grid and the probe. Specific tools (procured from Hummingbird Scientific) for the holder were also brought into the glove box to ensure damage-free disassembly/assembly of the holder.

For all experiments, Li_3PS_4:0.5LiI material was loaded onto the half-grid using the procedure

described for ex-situ TEM. The material loaded half-grid was then assembled into the holder component designed for the half-grid.

The W probe was converted into a lithium (Li) coated W probe for our applications, as follows. Li metal foil (MTI Corporation) was first cleaned by mechanical scraping of the foil surfaces using the plastic cap of a standard 20 ml glass vial (VWR). This scraped Li foil piece was placed on top of a 100-micron thick nickel (Ni) foil (Alfa Aesar) which was contained within a glass petri dish (VWR). The petri dish, along with the Ni and Li foil materials were then heated using a hot plate until the Li was observed to melt at which point the W probe was very gently dipped into the molten Li to procure the Li coated W probe. The dipping was accomplished by bringing the molten Li into contact with the probe, not vice-versa, to ensure safety of the fragile probe.

The holder was now completely reassembled within the glove box and the holder tip (containing the material loaded half-grid and Li probe components) was secured for air-free transfer from the glove box by using a customized air-free holder cap. Once secure with this cap, the holder was removed from the glove box using standard protocols and immediately moved to the TEM for loading.

The holder was loaded into the TEM while the air-lock for the TEM holder vented either nitrogen or argon gas to ensure air-free entry of the holder into the TEM. The custom air-free holder cap was removed from the holder at the TEM point of entry immediately prior to loading the holder into the TEM and pumping it down instantly to minimize sample exposure to air during this process. The total time that the sample was exposed to air was on the order of 5 to 10 seconds.

Once the holder was pumped down in the TEM, a suitable Li3PS4:0.5LiI sample was located

on the edge of the half-grid closest to the Li probe, and the Li probe was moved into position to contact this sample using manual and electronic adjustments to the probe via Hummingbird Scientific software. Upon contact, the noted in-situ TEM electrochemical experiments in the manuscript were carried out using a Bio-Logic SP-200 Potentiostat.
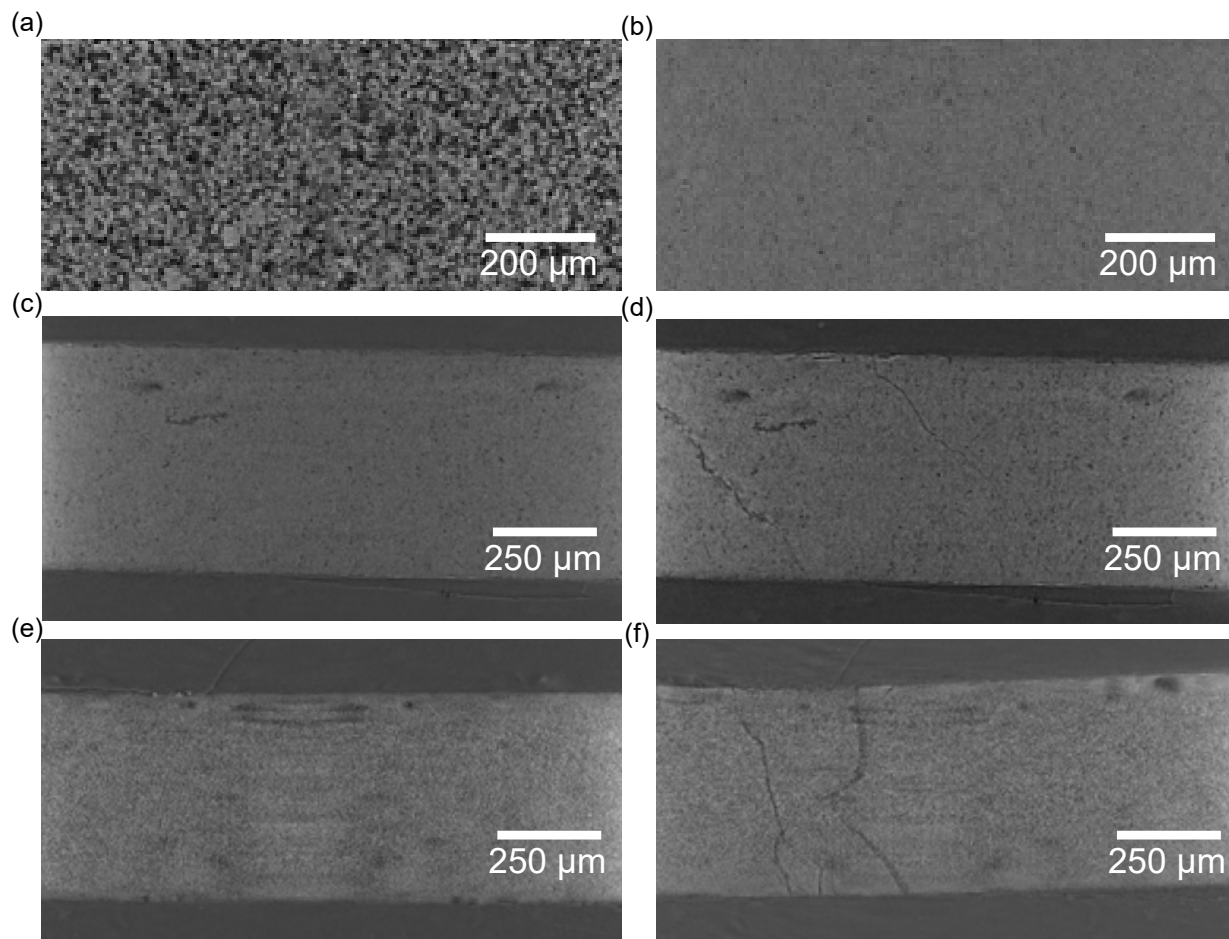
Fig S 1: Section of a reconstruction image for (a) amorphous LPS kept in contact with Li for extended duration (>5 hours) (b) amorphous LPS in contact with Li imaged within 15 min of cell assembly. Extended contact with Li metal shows decomposition of the LPS material into a highly porous material. Full cross-section image of Li|SE|Li cell assembled with A-LPS material in (c) pristine and (d) failed state and LiI–AN material in (e) prisitne and (f) failed state. No drastic variation in the microstructure is evidenced similar to that seen in the sample with extended contact (a). This allows for reliable interpretation of the data as electrochemistry driven material transformation as compared to the thermodynamics driven material degradation.
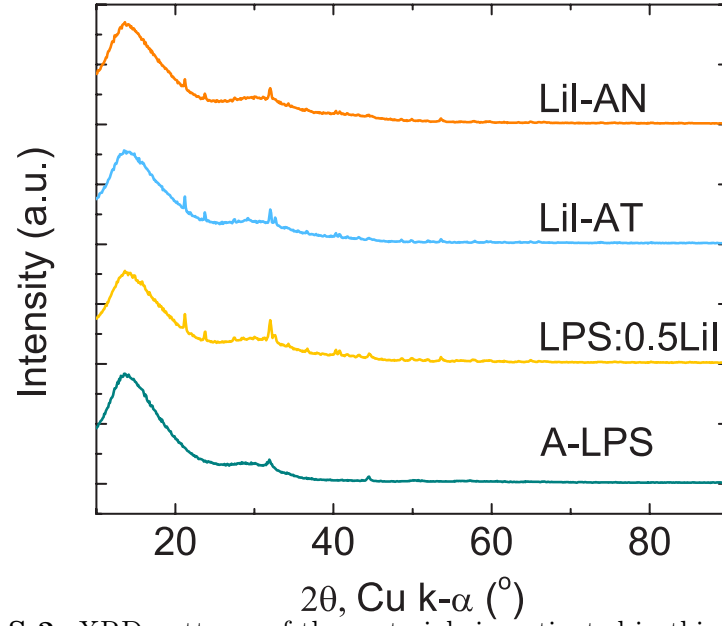
Fig S 2: XRD patterns of the materials investigated in this study.
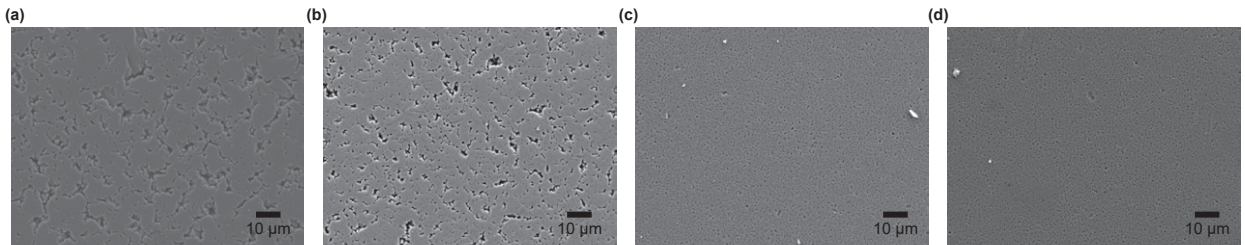
Fig S 3: SEM images highlighting differences in material microstructure of (a) A–LPS, (b) LPS:0.5LiI, (c) LiI–AT and (d) LiI–AN.
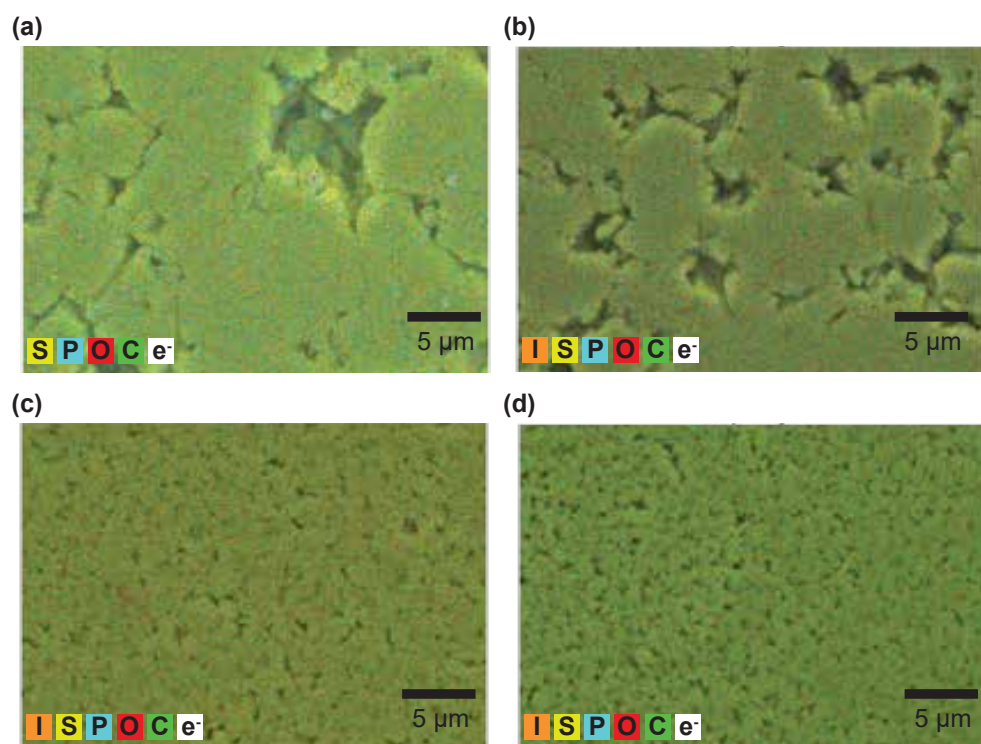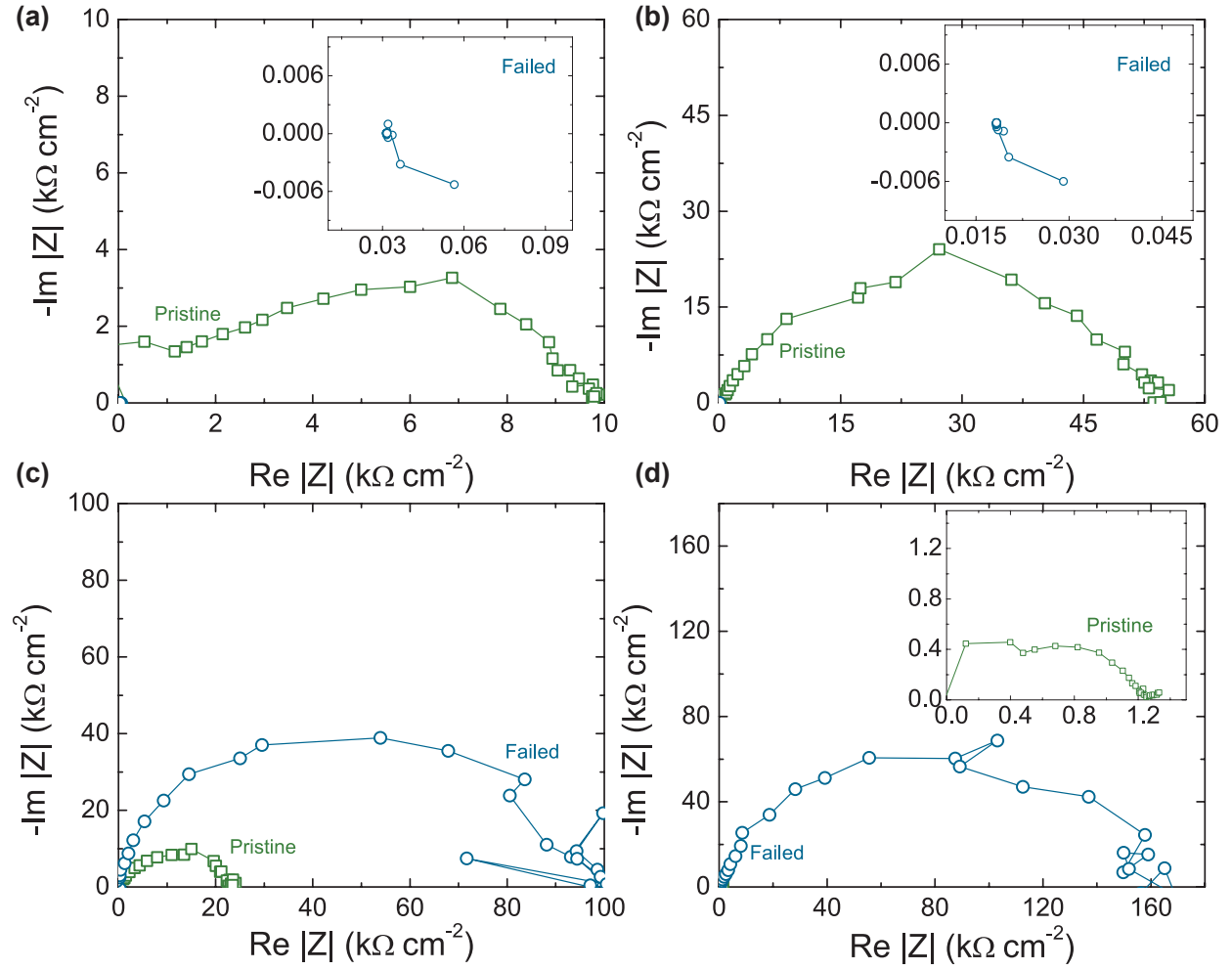
Fig S 4: EDS maps of (a)A–LPS, (b) LPS:0.5LiI, (c) LiI–AT, and (d) LiI–AN pellets. Iodine distribution is uniform for all the LiI containing samples.
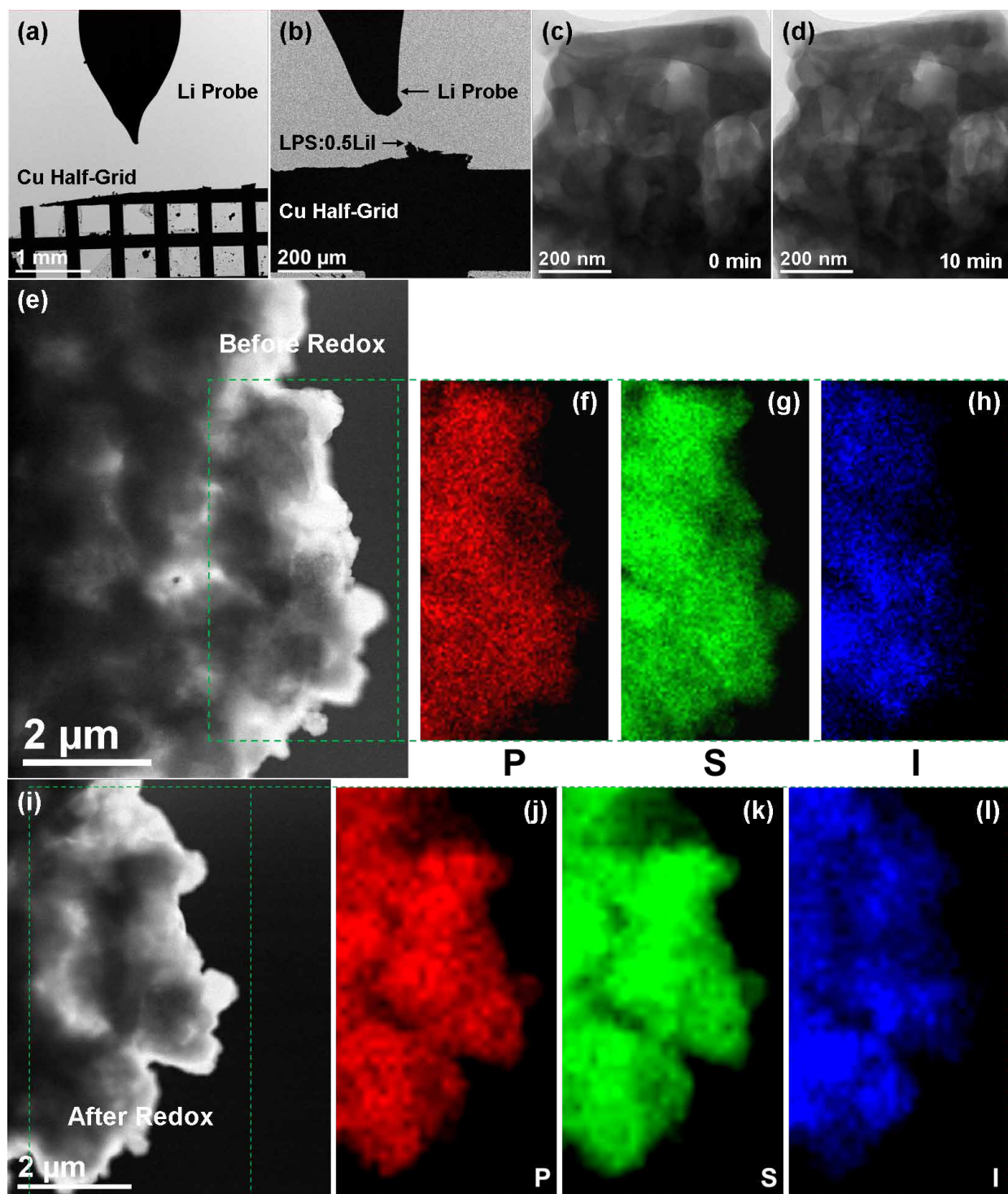
Fig S 5: (a) Low magnification *in situ* TEM image highlighting the Li probe and Cu half-grid within the in-situ TEM Nanomanipulator Holder, (b) low magnification *in situ* TEM image highlighting the position of LPS:0.5LiI on the Cu half-grid with respect to the Li probe, (c) TEM image of LPS:0.5LiI pristine material, (d) TEM image of LPS:0.5LiI pristine material after exposure to the electron beam in the HAADF STEM for 10 minutes, (e) *in situ* HAADF STEM image of LPS:0.5LiI prior to *in situ* electrochemical Li plating/stripping experiments performed in Figure 2, (f), (g), (h) phosphorus, sulfur and iodine EDS maps of LPS:0.5LiI prior to *in situ* electrochemical Li plating/stripping experiments performed in Figure 2 respectively, (i) *in situ* HAADF STEM image of LPS:0.5LiI after in-situ electrochemical Li plating/stripping experiments performed in Figure 2, (j), (k), (l) phosphorus, sulfur and iodine EDS maps of LPS:0.5LiI after *in situ* electrochemical Li plating/stripping experiments performed in Figure 2 respectively.
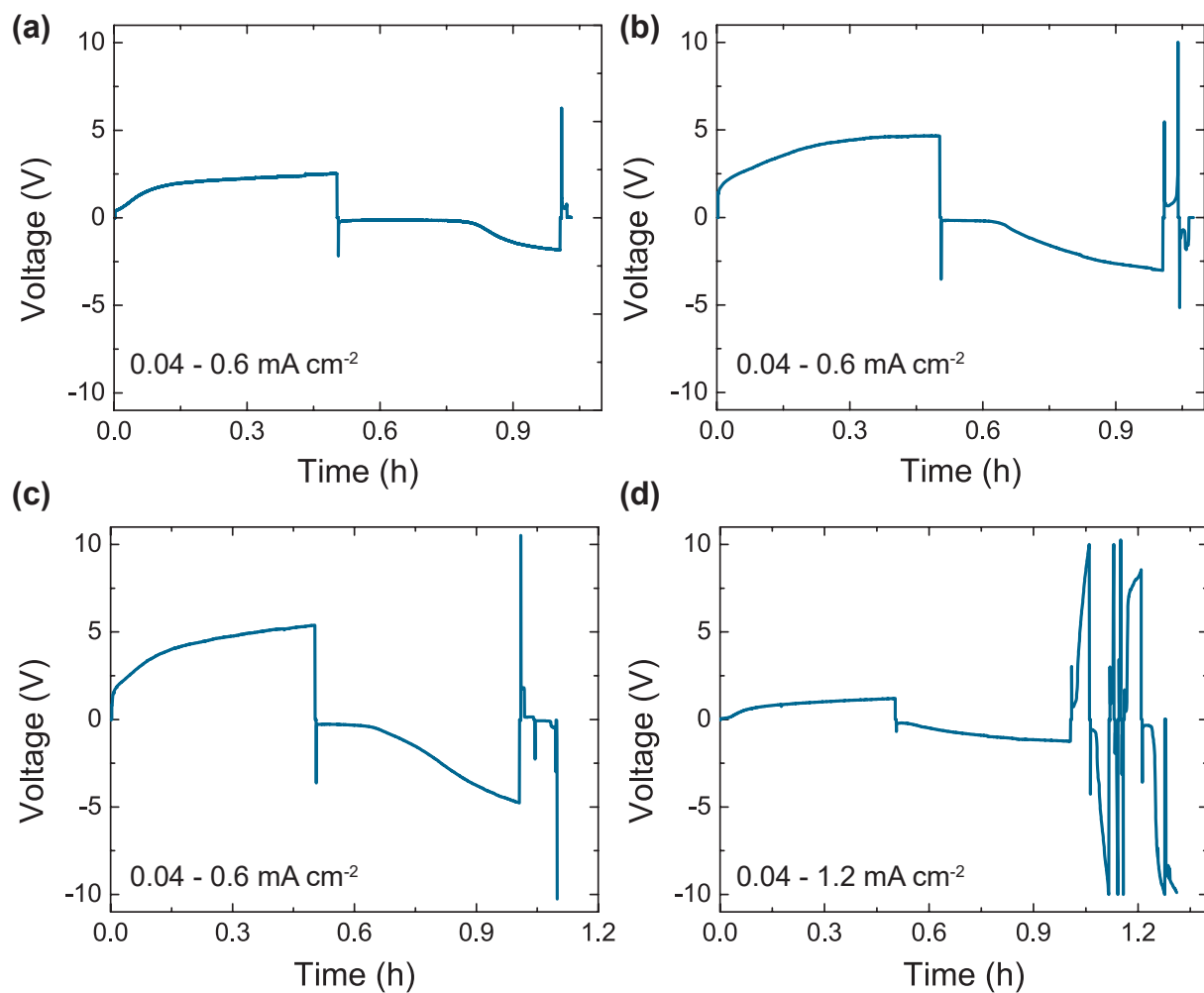
Fig S 6: Polarization profiles for *in situ* cells run for (a) A–LPS, (b) LPS:0.5LiI, (c) LiI–AT and (d) LiI–AN. The current density employed for the tests are indicated on the graphs. All testing was carried out at room temperature.

Fig S 7: AC impedance spectroscopy for as-assembled and cycled *in situ* cells for (a) A–LPS, (b) LPS:0.5LiI, (c) LiI–AT and (d) LiI–AN. All testing was carried out at room temperature.
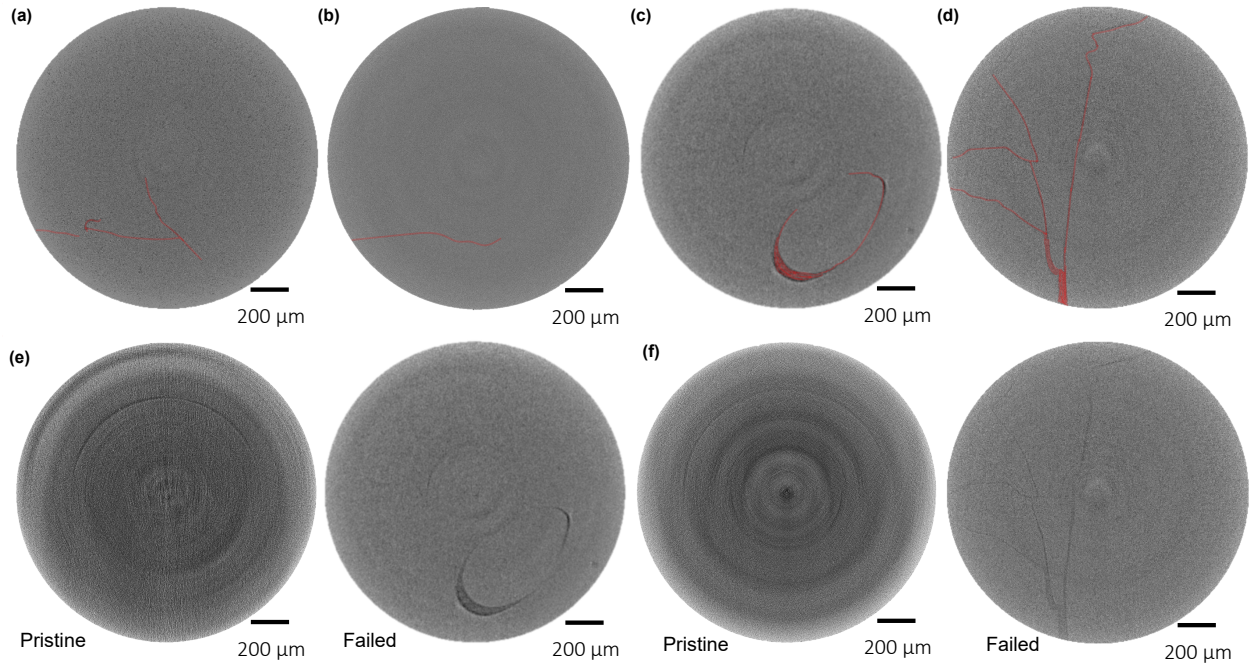
Fig S 8: Example reconstruction slices for (a) A–LPS, (b) LPS:0.5LiI, and (c) LiI–AT. For A–LPS and LiI–AT. The crack features in each slice are highlighted in red. Identifcal cross-section in prsitine and failed sample for LiI-AT and LiI–AN are also shown in (e) and (f) respectively. Crack features are not highlighted to enable visualization of cracks in as-reconstructed images.
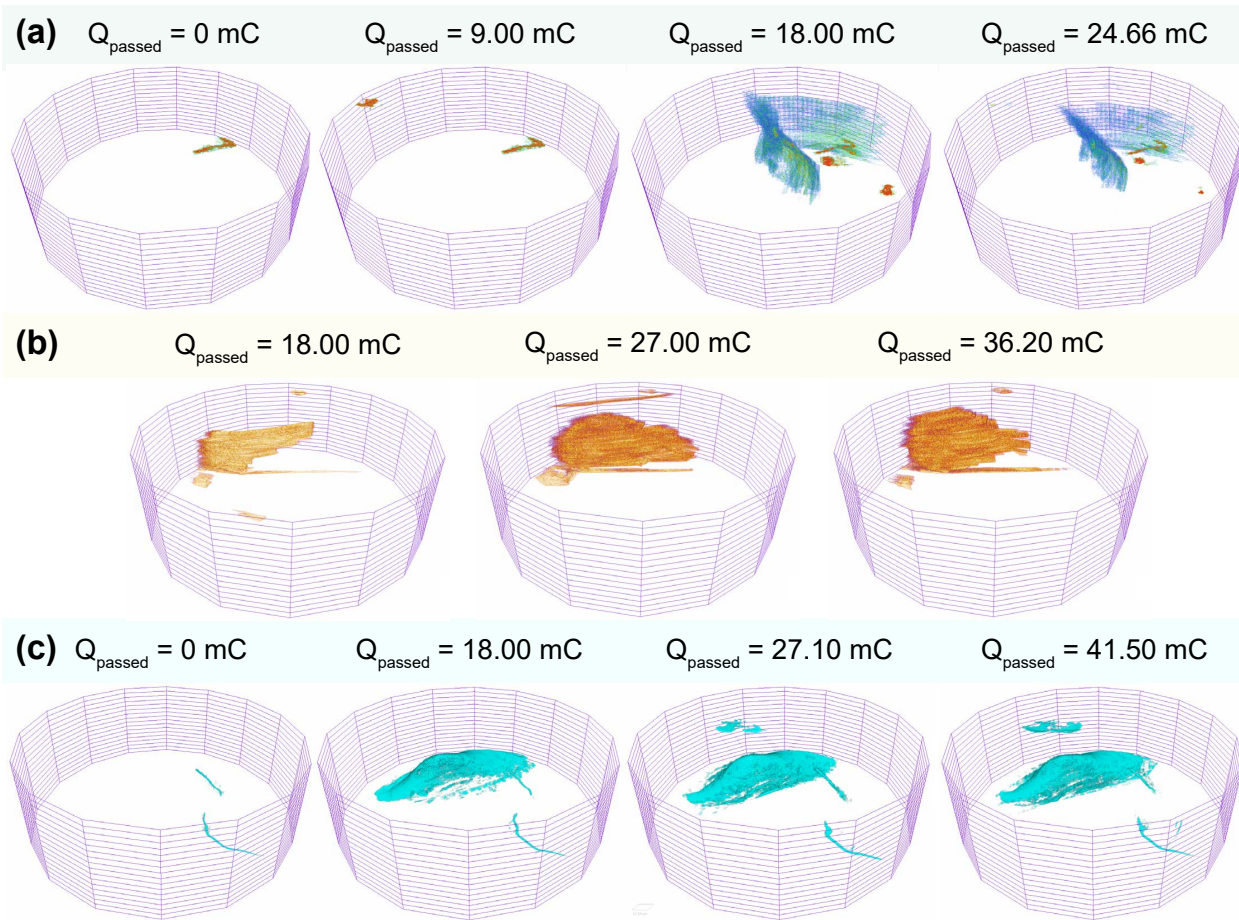
Fig S 9: Crack propagation at various plating, stripping steps for (a) A–LPS, (b) LPS:0.5LiI, and (c) LiI–AT. For A–LPS and LiI–AT features are shown at $Q_{passed}=0$ as these samples showed these microstructural features which are distinct from the general porosity of the sample.
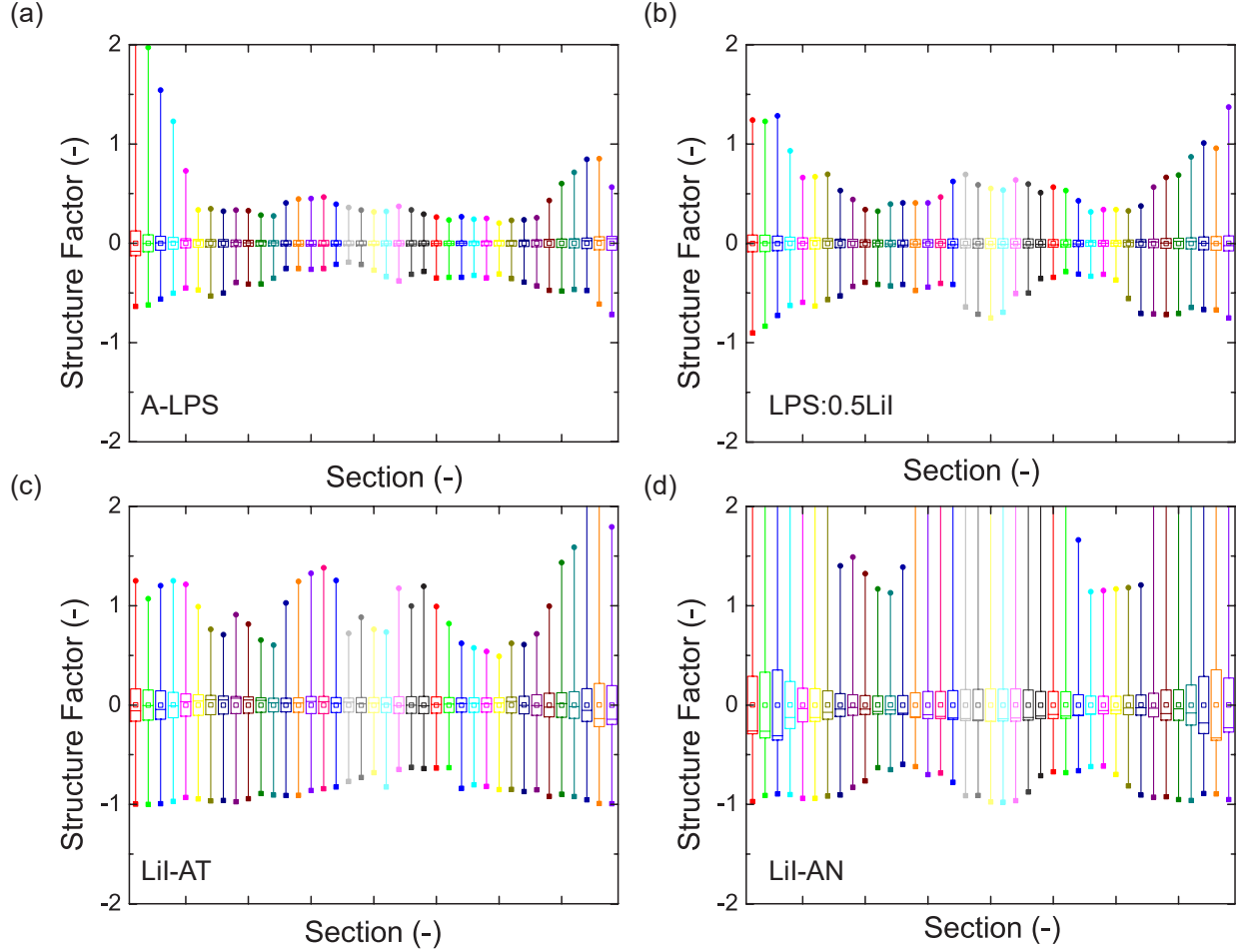
Fig S 10: Statistics on porosity factor calculated in the through-plane direction across section of the solid electrolyte. The images are for (a) A-LPS, (b) LPS:0.5LiI, (c) LiI–AT, and (d) LiI–AN. The images shows mean of each section, with a median line and a box marking the standard deviation. Maximum and minimum porosity factor are also plotted. porosity factors are calculated on a $30x30x30$ μm^3 sub-volumes across the cross-section of the electrolyte. The statistics for a single section included porosity factors for all the sub-volumes in an electrolyte cross-section, i.e. $\approx 24x30$ porosity factors.
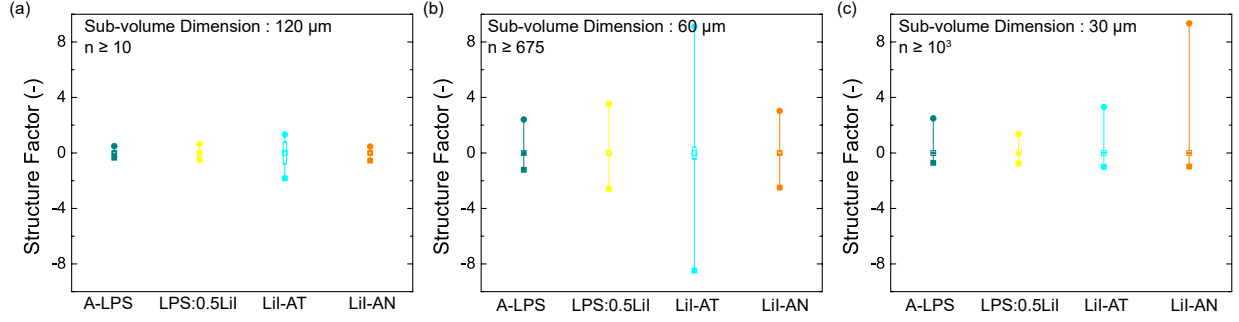
Fig S 11: Statistics on porosity factor calculated in the in-plane direction along the direction of ion transport through the thickness of the solid electrolyte. The raw projections were used for this calculations to eliminate the errors from binarization. The images shows mean of each section, with a median line and a box marking the standard deviation. Maximum and minimum porosity factor are also plotted. porosity factors are calculated on sub-volumes of sizes (a) 30x30x30 μm^3, (b) 60x60x60 μm^3, and (c) 30x30x30 μm^3. The statistics for a single sub-volume size includes porosity factors for all the sub-volumes in an electrolyte cross-section. The approximate number of individual measurements are noted in the graph. Moving to larger sub-volumes normalizes the local heterogeneity and a uniform spread of porosity factors is observed.
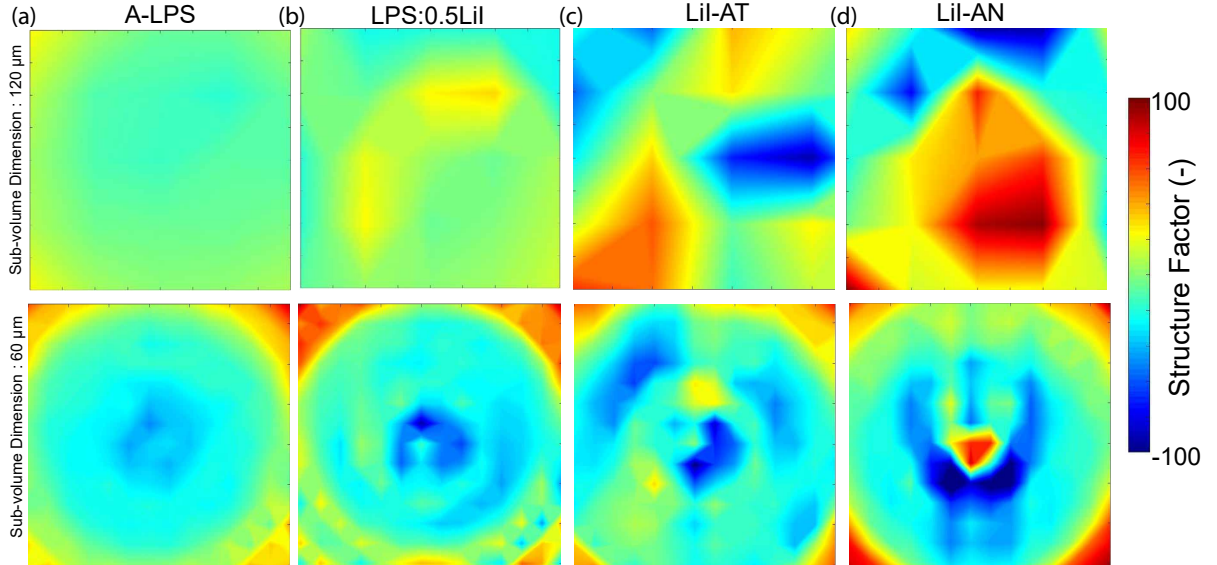
Fig S 12: Porosity factor calculated in the in-plane direction along the direction of ion transport through the thickness of the solid electrolyte. The raw projections were used for this calculations to eliminate the errors from binarization. As the full reconstruction was used, the corners of the image are extraneous. The images are for (a) A-LPS, (b) LPS:0.5LiI, (c) LiI–AT, and (d) LiI–AN for 60x60x60 μm^3 and 120x120x120 μm^3 sub-volume size.
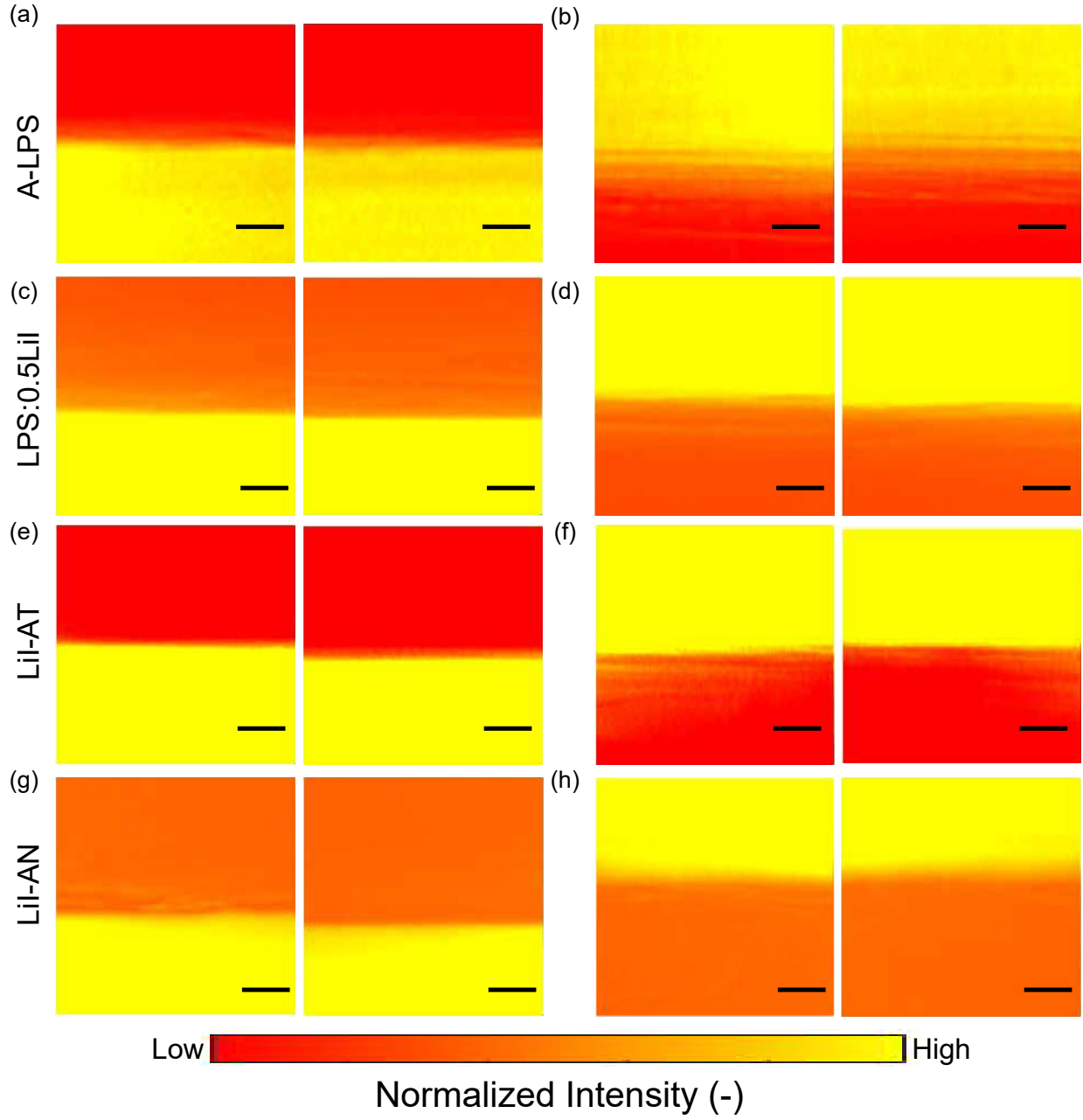
Fig S 13: Statistics on interfacial intensity map at the solid|solid interface. Intensity map are for (a) top Li|SE and (b) bottom SE|Li interfaces in A-LPS, (c) top Li|SE and (d) bottom SE|Li interfaces in LPS-LiI, (e) top Li|SE and (f) bottom SE|Li interfaces in LiI-AT, (g) top Li|SE and (g) bottom SE|Li interfaces in LiI-AN. All the scale bars in the figure are 30 μm.
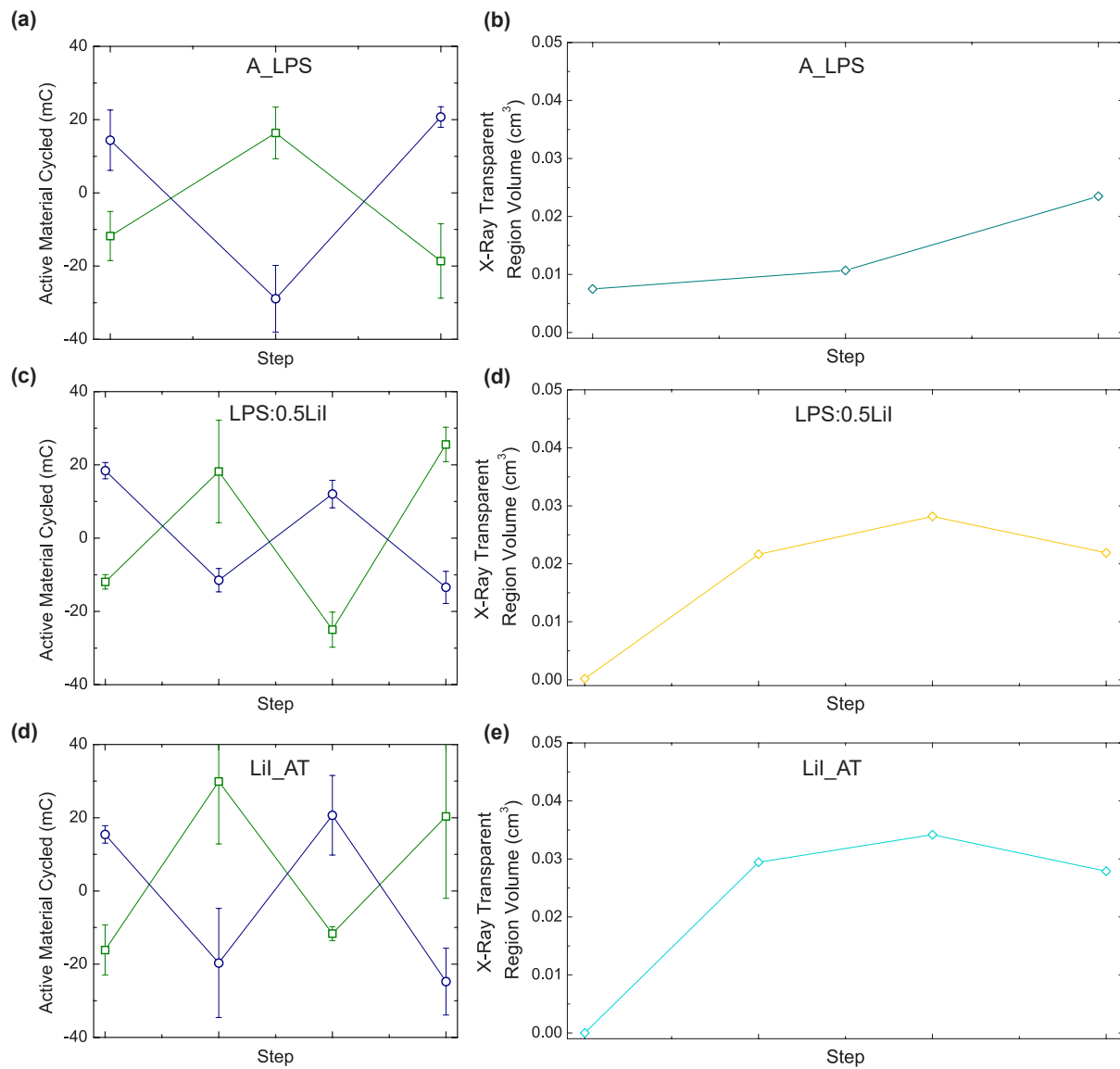
Fig S 14: Active material cycled during plating and stripping cycles for (a) A–LPS, (c) LPS–LiI and (d) LiI–AT. Variation in X-ray transparent region volume during plating and stripping cycles for (a) A–LPS, (c) LPS–LiI and (d) LiI–AT

17